



PONTIFICIA UNIVERSIDAD CATÓLICA DE CHILE
FACULTAD DE FÍSICA
INSTITUTO DE ASTROFÍSICA

Characterizing the Fe $K\alpha$ line variability in a large sample of AGN

BY

CAROLINA PAZ ANDONIE BAHAMONDES

Tesis presentada a la Facultad de Física de la Pontificia Universidad Católica de Chile, para optar
al grado académico de Magíster en Astrofísica.

SUPERVISOR : Dr. Franz Bauer

CORRECTORS : Dr. Claudio Ricci

CORRECTORS : Dr. Nelson Padilla

July 10th, 2020

Santiago, Chile

©2020, Carolina Andonie

Declaration

©2020, Carolina Andonie

Se autoriza la reproducción total o parcial, con fines académicos, por cualquier medio o procedimiento, incluyendo la cita bibliográfica del documento.

Acknowledgements

Hacer el magíster en Astrofísica no fue una tarea fácil y hay muchas personas que me acompañaron e hicieron que esta fuera una gran experiencia.

Primero que todo, agradecer a los profesores Claudio Ricci, Ezequiel Treister y Franz Bauer, por guiarme durante estos años de trabajo, por haber compartido sus conocimientos conmigo y haber contribuido de forma importante en haber terminado esta etapa de forma exitosa.

Estos 2 años no hubieran sido tan entretenidos sin la compañía de Cesar Calderon, Camila Órdenes, Jonathan Quirola, Felipe Espinoza, Carlos Orquera, Dusán Tubín, Andrés Scherer y Katherin Joachimi. Esas tardes de conversaciones y (no) trabajo hacían que fuera feliz a la universidad todos los días. Para que hablar de la mejor oficina con Felipe Rojas, Goran Doll y Gonzalo Prieto, las conversaciones (y cahuines) con un cafecito después de almuerzo eran geniales. También agradecer a Paula Sanchez por haber compartido su gran conocimiento conmigo todas las veces que le pedí ayuda, y por su compañía en uno de los momentos más difíciles de mi magister, que fue dar mi primera charla en una conferencia. Habría sido genial vernos durante mi último semestre, pero el coronavirus no lo hizo posible. Siempre estaré agradecida por lo buenos momentos que pasamos.

También quiero agradecer a mis padres por siempre apoyarme en esta loca idea de ser astrónoma, y por ser parte de mis logros.

Por último, quiero agradecer a Pablo por ser un gran compañero de vida, por acompañarme, ayudarme, y vivir conmigo las etapas más importantes que me han tocado pasar.

Contents

1	Introduction	12
1.1	Anatomy of AGN	13
1.2	AGN classification and Unified Model	14
1.3	X-ray emission in AGN and the Fe $K\alpha$ line	16
1.4	Motivation and goals	17
2	Data analysis	22
2.1	Observations and data reduction	22
2.1.1	Sample selection	22
2.1.2	<i>Chandra</i> X-ray Observatory	23
2.1.3	<i>XMM-Newton</i>	26
2.2	Spectral analysis	27
2.2.1	Spectral fitting	27
2.2.2	The pileup problem and its solution	27
2.2.3	Light curves analysis	31
2.3	Imaging analysis	32
3	<i>Chandra</i> and <i>XMM-Newton</i> spectral results	34
3.1	Fe $K\alpha$ line and 2–10 keV continuum behavior	34
3.2	$F_{6.4 \text{ keV}}-F_{2-10 \text{ keV}}$ slopes constrain problem	41
3.3	$F_{6.4 \text{ keV}}-F_{2-10 \text{ keV}}$ slopes compared with AGN and host galaxy properties	41
4	<i>Chandra</i> Imaging results	47
4.1	<i>Chandra</i> PSF caveats	47

4.2	Empirical PSF and its comparison with our sources	48
4.3	The case of NGC 1068	53
5	Discussion	55
6	Conclusions and future work	61
	Bibliography	67
A	Light curves	68
B	Radial profiles	72

List of Tables

3.1 Summary of the well-constrained $F_{6.4 \text{ keV}}-F_{2-10 \text{ keV}}$ slopes, the maximum light curve timespan of the observations per source, the P_{var} parameters obtained for the Fe $K\alpha$ line and 2–10 keV continuum light curves of each source and whether the sources are radio-loud AGN. The sources with a star (*) have a slope consistent with one, but do not have highly significant variable light curves for the Fe $K\alpha$ line fluxes. The sources with two stars (**) have a beamed jet (information obtained from Koss et al. (2018)) . 2MASXJ11 and 2MASXJ23 correspond to 2MASXJ11315154-1231587 and 2MASXJ23444387-4243124, respectively. 36

5.1 Upper limits for the reflecting clouds emitting Fe $K\alpha$ photons found with the spectral and imaging analysis. 57

List of Figures

1.1	Unification model for radio-loud and radio-quiet AGN (Beckmann & Shrader 2012). The scheme shows the different types of AGN depending on the orientation, presence or absence of the jet, and accretion power.	15
1.2	AGN spectra with a $N_H \sim 10^{24} \text{ cm}^{-2}$. Several important X-ray features are depicted, such as the thermal emission (not mentioned in this work), the Fe $K\alpha$ line, the Reflection hump (or Compton hump), the transmitted power-law and the scattered component. The relative normalizations in this figure are illustrative only. Figure courtesy of Claudio Ricci.	18
1.3	Figure reproduced from Iwasawa et al. (1996), showing the 3-10 keV count rate versus the intensity of the narrow component of the Fe $K\alpha$ line (first panel), the EW of the narrow component of the Fe $K\alpha$ line (second panel), the intensity of the broad component of the Fe $K\alpha$ line (third panel) and the EW of the broad component of the Fe $K\alpha$ line (fourth panel).	19
1.4	Figure from Bianchi et al. (2007). The IT effect: Fe $K\alpha$ line EW against 2–10 keV X-ray luminosity for 157 radio-quiet Type 1 AGN. The different symbols refer to the classification of the objects, based on their absolute magnitude and $H\beta$ FWHM: NLSY, narrow-line Seyfert 1; BLSY, broad-line Seyfert 1; NCSY, not-classified Seyfert 1 (no $H\beta$ FWHM measure available); NLQ, narrow-line quasar; BLQ, broad-line quasar; NCQ, not-classified quasar (no $H\beta$ FWHM measure available). The analytical expression for the best fit line is reported on the top.	20

-
- 2.1 HETG observation of Capella, ObsID 1318, obtained from Chapter 8 of the *Chandra* Proposer's Observatory Guide, Cycle 22. The top panel shows the raw zeroth-order image (similar to a normal ACIS observation) in the CCD S3 and an X-shaped feature, which is the dispersed HEG and MEG spectra (first-order and second-order spectra). The second panel shows an aspect corrected image after selection applied only to include the zeroth and first-order events. The last three panels show zoom-in views of the MEG -1 -order spectrum, where the numbers are the wavelengths of the emission lines in the spectra, in Angstrom units. 24
- 2.2 ACIS observation of the galaxy Centaurus A Obsid 20794. The thin diagonal line crossing the source is the readout streak. The observation is very affected by saturation, producing a hole in the center of the image. We can also see off-nuclear X-ray sources associated with the galaxy and background AGN, as well as a clumpy jet; we much take care to avoid these features for some analyses. 25
- 2.3 2–10 keV spectrum for the Type 2 AGN Centaurus A, obsid 1601, fitted by the model described in Eq.2.1. The spectrum is attenuated by the strong absorption. The unique notorious emission line is the Fe $K\alpha$ line at 6.4 keV. 28
- 2.4 Example of the encircled energy at 1 keV versus circular extraction aperture radius for ACIS observation of the point source PG1634-706 (ObsID 1269). The encircled energy depends on the energy and off-axis angle. 29
- 2.5 Calibration constants between the *Chandra* HEG 1st order and ACIS/HETG 0th order $3''$ – $5''$ annular spectra. The upper panel shows all the calibration constants, and the lower panel shows the calibration constants consistent with the "floor" found at 0.424 ± 0.00507 , marked by a red dashed line. 30
- 2.6 Merged image of all the ACIS observation available for Circinus Galaxy. The right image is the original, and the left image is after removing all the point sources. The green circles represent the annular regions used for the radial profiles extraction, using a logarithmic binning. 33

3.1	Fe $K\alpha$ line flux ($F_{6.4 \text{ keV}}$) against 2–10 keV continuum flux ($F_{2-10 \text{ keV}}$), for the sources with well-constrained $F_{6.4 \text{ keV}}-F_{2-10 \text{ keV}}$ slopes. In the subplots, the green stars are the <i>Chandra</i> HEG spectra, the black stars are the <i>Chandra</i> ACIS 3''-5'' annular spectra, the blue stars are the 1.5'' circular ACIS spectra and the red stars are the <i>XMM-Newton</i> spectra. The values for the slopes are summarized in Figure 3.2. The flux units are $\text{erg cm}^{-2} \text{ s}^{-1}$	37
3.2	$F_{6.4 \text{ keV}}-F_{2-10 \text{ keV}}$ slopes (m) for 19 sources with well-constrained values	38
3.3	Light curves for the 2–10 keV continuum (a) and Fe $K\alpha$ line (b) fluxes for the galaxy Centaurus A. The green and black stars denote fluxes measured from the <i>Chandra</i> HEG 1st order spectra and <i>Chandra</i> ACIS 3''–5'' annular spectra, respectively.	39
3.4	Light curves for the 2–10 keV continuum flux (a) and Fe $K\alpha$ line fluxes (b) for the galaxy NGC 3516. The green and black stars are fluxes measured from the <i>Chandra</i> HEG spectra and <i>Chandra</i> ACIS 3''-5'' annular spectra, respectively.	39
3.5	Light curves for the 2–10 keV continuum flux (a) and Fe $K\alpha$ line fluxes (b) for the galaxy NGC 1275. The green and black stars are fluxes measured from the <i>Chandra</i> HEG spectra and <i>Chandra</i> ACIS 3''-5'' annular spectra, respectively.	40
3.6	Comparison between the size of the $F_{6.4 \text{ keV}}-F_{2-10 \text{ keV}}$ slopes errorbars and the number of observations (a), the maximum light curve timespan (b) and the non detected Fe $K\alpha$ line flux measurements versus total measurements (c). The orange line is the linear fit of the points and m is the slope of the line obtained for each plot.	42
3.7	Comparison between the $F_{6.4 \text{ keV}}-F_{2-10 \text{ keV}}$ slopes and T_{lc} , which is the ratio between the maximum light curve timespan and the sublimation radius, for all the sources with bolometric luminosity measured.	44
3.8	Comparison of the $F_{6.4 \text{ keV}}-F_{2-10 \text{ keV}}$ slopes with respect to (a) the Supermassive Black Hole mass, (b) the Gini index, (c) the Eddington ratio, (d) the equatorial column density, and (e) the AGN type. For the first four plots, a linear regression was made between the slopes and the parameter. The slope is indicated in the legend of each plot.	45

4.1	Comparison between real and simulated radial profiles for the X-ray binary HERX1. Panels (a) and (b) show radial profiles for the 6.2–6.5 keV and 5–6 keV ranges, respectively. The errors of the real profiles denote 99% confidence, while the errors of the simulated profiles are 97% confidence.	48
4.2	Radial profiles for each quadrant of the images of HERX1, in the 6.2–6.5 keV energy range. q1, q2, q3, and q4 are equivalent to quadrant I, quadrant II, quadrant III, and quadrant IV in the coordinate plane. The errors plotted are 97% confidence.	49
4.3	Comparison between the 6.2–6.5 keV radial profile of HERX1 (blue points) and our sources with well constrained $F_{6.4 \text{ keV}}-F_{2-10 \text{ keV}}$ slopes (red points). The green dotted line on each plot represents the free pileup radii used to choose the normalization flux for each profile.	51
4.4	Radial profiles for each quadrant of the images, for all the sources with well constrained $F_{6.4 \text{ keV}}-F_{2-10 \text{ keV}}$ slopes (except the ones with difficult contamination subtraction). The profiles are for the flux in the 6.2–6.5 keV range. q1, q2, q3, and q4 are equivalent to quadrant I, quadrant II, quadrant III, and quadrant IV. The errors plotted are 99% confidence.	52
4.5	Radial profiles of the 6.2–6.5 keV flux of NGC 1068. The panel (a) shows the comparison between the profile of HERX1 and NGC 1068. The profiles are normalized with the flux at the free pileup radii marked by the green line. The panel (b) shows the 6.2–6.5 keV radial profiles for each quadrant of the images at 97.7% confidence error.	54
4.6	<i>Chandra</i> image for the 2–10 keV emission of NGC 1068. The green circle marks the inner 20'' region.	54
A.1	Light curves for the 2–10 keV continuum flux ($F_{2-10 \text{ keV}}$) for the sources with well-constrained $F_{6.4 \text{ keV}}-F_{2-10 \text{ keV}}$ slopes. In the subplots, the green stars are the <i>Chandra</i> HEG spectra, the black stars are the <i>Chandra</i> ACIS 3''–5'' annular spectra, the blue stars are the 1.5'' circular ACIS spectra and the red stars are the <i>XMM-Newton</i> spectra. The unities of the flux are $\text{erg cm}^{-2} \text{ s}^{-1}$	69

A.2	Light curves for the Fe $K\alpha$ line flux ($F_{2-10\text{ keV}}$) for the sources with well-constrained $F_{6.4\text{ keV}}-F_{2-10\text{ keV}}$. In the subplots, the green stars are the <i>Chandra</i> HEG spectra, the black stars are the <i>Chandra</i> ACIS 3''–5'' annular spectra, the blue stars are the 1.5'' circular ACIS spectra and the red stars are the <i>XMM-Newton</i> spectra. The unities of the flux are $\text{erg cm}^{-2} \text{s}^{-1}$	70
A.3	Same as Figure 3.1 but for the sources with unconstrained $F_{6.4\text{ keV}}-F_{2-10\text{ keV}}$ slopes. The value of the slope (m) is in the legend of each source	71
B.1	Radial profiles for each quadrant of the images of all the sources with well-constrained $F_{6.4\text{ keV}}-F_{2-10\text{ keV}}$ slopes (except the ones with difficult contamination subtraction). The profiles are for the flux in the 2.5–3 keV range. q1, q2, q3 and q4 are equivalent to quadrant I, quadrant II, quadrant III and quadrant IV. The errors plotted are 3-sigma confidence.	73
B.2	Same as Figure B.1, but for the Fe $K\alpha$ line photons	74
B.3	Image for the Fe $K\alpha$ line photon of NGC 4051. The quadrants are pointed in the image. The circles mark radii of 2'' and 4''.	75
B.4	Radial profiles for each quadrant of the images of NGC 1068, for different energy ranges, going from 2.5–3 keV to 6.5–6.8 keV	76

Resumen

Varios Nucleos Activos de Galaxias (AGN) han mostrado variabilidad en su emisión en rayos X, en particular en el continuo entre 2–10 keV y en la línea de emisión de Hierro en 6.4 keV (Fe $K\alpha$). La línea Fe $K\alpha$ es una característica obicua en el espectro de los AGN y es producida por procesos de reflexión entre el continuo y la materia neutra que rodea el Agujero Negro Supermasivo (SMBH) que se encuentra en el centro del AGN. Varios estudios han constreñido la ubicación y el tamaño de las nubes reflectantes en algunos AGN estudiando la reacción de la línea a variaciones del continuo. En este trabajo, constreñimos la relación entre la línea Fe $K\alpha$ y el continuo para 19 fuentes, usando datos de los observatorios *Chandra* y *XMM-Newton*. Encontramos diferentes comportamientos, los cuales se pueden clasificar en 3 casos. Primero, en algunos AGN el flujo de la línea está dominado por nubes reflectantes ubicadas cerca de la corona de rayos X, como en el disco de acreción o la región de líneas anchas, por lo que la línea reacciona rápido frente a variaciones del continuum en las escalas de tiempo de las observaciones. Para estas fuentes, proporcionamos un límite superior para la región reflectiva. Segundo, en otros casos, la línea Fe $K\alpha$ reacciona levemente frente a las variaciones del continuo, por lo que los flujos no están correlados, sugiriendo que las nubes reflectantes están localizadas mucho más lejos de la corona, como en el toro polvoriento. El último y tercer caso, son AGN que muestran variabilidad en el continuo y en la línea, pero los flujos no están correlacionados, indicando un escenario más complejo. Encontramos una leve correlación entre la relación Fe $K\alpha$ -continuo y la masa del SMBH, indicando que a mayores masas las nubes reflectantes estarían ubicadas más cerca de la corona de rayos X. Para complementar los resultados espectrales, analizamos las imágenes de las observaciones de *Chandra* para ver si la emisión Fe $K\alpha$ es extendida espacialmente. Encontramos que 14/15 fuentes analizadas son consistentes con una fuente puntual, para las cuales pudimos entregar un límite superior de la región reflectante emitiendo fotones Fe $K\alpha$, equivalente a la resolución espacial de *Chandra* (~ 1.21 hasta 1419 pc).

Abstract

Several Active Galactic Nuclei (AGN) have shown variability in the X-ray band, in particular the 2–10 keV continuum flux and the Iron $K\alpha$ (Fe $K\alpha$) line at 6.4 keV. The Fe $K\alpha$ line is a universal feature in the X-ray spectra of AGN, which is produced by reflection processes between the continuum and circumnuclear neutral matter, therefore it is very important to study the environment of the central Supermassive Black Hole (SMBH). Several works have been able to constrain the location and size of reflecting clouds in some AGN by studying the reaction of the Fe $K\alpha$ line flux to variations of the primary emission. In this work, we constrained the relation between the Fe $K\alpha$ line and the 2–10 keV continuum for 19 sources, using data from the *Chandra* and *XMM-Newton* observatories. We found a wide variety of behaviors, which are classified in 3 cases. First, in some AGN the Fe $K\alpha$ line flux is dominated by reflecting clouds located near to the X-ray emission sources, as the accretion disk or the broad-line region, therefore the line reacts quickly to continuum variation in the observations timescales. For these sources, we provided an upper limit for the reflecting region. Second, the reaction of the Fe $K\alpha$ line to continuum variation is mild, suggesting that the reflecting clouds are located at larger scales, in the dusty torus, but alternative explanations are also possible. And third, some AGN show variability in both Fe $K\alpha$ line and continuum, but the fluxes are not correlated, suggesting a more complex picture. Additionally, we looked for correlations with some AGN and host galaxy properties and only found a mild correlation between the Fe $K\alpha$ line-continuum relation and the SMBH mass, indicating that at higher masses the reflecting clouds may be located nearer to the X-ray corona. To complement the spectral results, we made an imaging analysis of the *Chandra* observations to check if the Fe $K\alpha$ emission is spatially extended. We found that 14/15 sources are consistent with being point-like. Using this fact, we provided an upper limit for the reflecting clouds emitting Fe $K\alpha$ photons equivalent to the *Chandra* imaging resolution (~ 1.21 to 1419 pc).

Chapter 1

Introduction

Active Galactic Nuclei (AGN) are strongly accreting Supermassive Black Holes (SMBH) at the center of galaxies that emit a large luminosity, across much of the electromagnetic spectrum. The galaxy hosting the AGN is considered an "active" galaxy and the mass of the central SMBH is in the $10^6 - 10^{10} M_{\odot}$ range. This huge quantity of mass transforms the potential energy of the accreting mass into radiation, mainly from UV to near-infrared energies. This radiation may be further reprocessed into the infrared band, while additional radio and X-ray wavelength contributions can arise through separate mechanisms.

A universal characteristic of AGN is its X-ray emission. While this only comprises between 1 – 10% of the total emission (e.g., Vasudevan & Fabian 2007; Lusso et al. 2010), the X-ray emission has a clear fundamental connection to the accretion disk (e.g., Steffen et al. 2006; Lusso et al. 2010; Just et al. 2007), and it is one of the wavebands where the AGN/galaxy contrast is highest, allowing a relatively complete AGN census (e.g., Brandt & Alexander 2015). The X-ray band allows us to probe important characteristics and physical processes of the AGN, which we describe below.

In this Chapter, we present the anatomy of AGN in Section 1.1) and the AGN classification and Unification in Section 1.2). We talk about the X-ray emission in AGN in Section 1.3) and lastly, we present the motivations and goals of this work in Section 1.4.

1.1 Anatomy of AGN

The main elements of AGN are the SMBH, the accretion disk, the dusty torus, the broad line region (BLR), the narrow line region (NLR), the corona and the jets.

The central engine of AGN is the SMBH located in the center of the galaxy. The Schwarzschild metric describes the space-time for a non-rotating black hole, where the radius from the singularity interior to which not even light can escape (i.e., the event horizon) is given by the so-called Schwarzschild radius:

$$r_g = \frac{2GM_{\text{BH}}}{c^2}, \quad (1.1)$$

where M_{BH} is the mass of the SMBH, G is the gravitational constant and c the speed of light.

Around the SMBH there is a disk of gas, called the accretion disk, formed by rotating gas which is falling onto the central SMBH. This accretion is responsible for the large luminosity observed. In AGN, the gas generally has a high angular momentum and collapses into a multi-temperature accretion disk, whereby each ring emits pseudo-blackbody radiation ($L(r) \propto \sigma T^4$), with a temperature profile which goes as $T(r) \propto r^{-3/4}$ (e.g., Shakura & Sunyaev 1973). On the other hand, for low angular momentum gas, the accretion is spherical and inefficient (e.g., Bondi 1952).

The broad-line region (BLR) is comprised of dense, photoionized clouds orbiting around the SMBH, located relatively close to the accretion disk, which produce broad emission lines in the AGN spectrum. The dynamical broadening of these lines is due to the deep gravitational potential of the SMBH, and hence can be used to measure its mass. Additionally, these lines can give us valuable information about the physical conditions of the environment of the SMBH. The BLR extends out to the dust sublimation radius, which traces the distance interior to which all the dust is sublimated into gas.

The corona is the region where the X-ray radiation is produced. This region is located within few r_g of the SMBH and is thought to be located above the accretion disk (e.g., Fabian et al. 2009; De Marco et al. 2013). The corona is formed by hot electrons, and produces the X-ray photons through inverse Comptonization with UV/optical photons coming from the accretion disk (e.g., Haardt & Maraschi 1991). This process is explained in more detail in section 1.3.

Beyond the BLR and dust sublimation lies the so-called dusty "torus" region. We do not know the exact geometry of this region, but it is typically represented by an optically and geometrically thick toroidal reprocessor (e.g., Ghisellini et al. 1994; Guainazzi et al. 2005). This toroidal component is a reprocessor of the UV/optical photons coming from the accretion disk, re-emitting them as thermal IR radiation. The torus is also thought to reprocess the X-ray photons coming from the corona, via Compton scattering of neutral matter.

At galactic scales, AGN possess a narrow-line region (NLR), comprised of dense photoionized clouds much further away from the SMBH, which produce narrow optical emission lines in the spectrum. It is believed to extend to hundreds of parsecs from the SMBH. By observing the spectrum of the NLR we are able to improve our understanding of different AGN components.

The last component is the jet, which is believed to form within a few r_g of the SMBH and extend out hundred of parsecs in many AGN, and even thousands to millions for some AGN. The jets are extremely energetic and highly collimated plasma (Blandford 2001), emit strongly in the radio band and are not present in all the AGN; as such they are important for AGN classification. The exact physical processes by which jets are formed and maintained is not completely understood and is an area of ongoing theoretical research.

1.2 AGN classification and Unified Model

AGN come in many flavors and it took many decades to connect the taxonomy to a few key parameters. The first and most fundamental parameters is the orientation of the AGN with respect to the observer's line of sight. The asymmetric structure of the AGN environment and geometry of the absorber imply that the amount of absorbing material varies with sight-line, such that we see different features from different orientations. A second important parameter is the radio emission, which is associated to the presence (radio-loud AGN) or absence (radio-quiet AGN) of a jet. Other important parameters are likely the SMBH mass and spin, and the accretion rate.

While only comprising 10% of AGN by number, the most enigmatic AGN are radio-loud. They present strong radio emission, and are classified as either radio galaxies (host dominant over nucleus), radio quasars (nucleus dominant over host) and radio blazars (nucleus relativistically beamed).

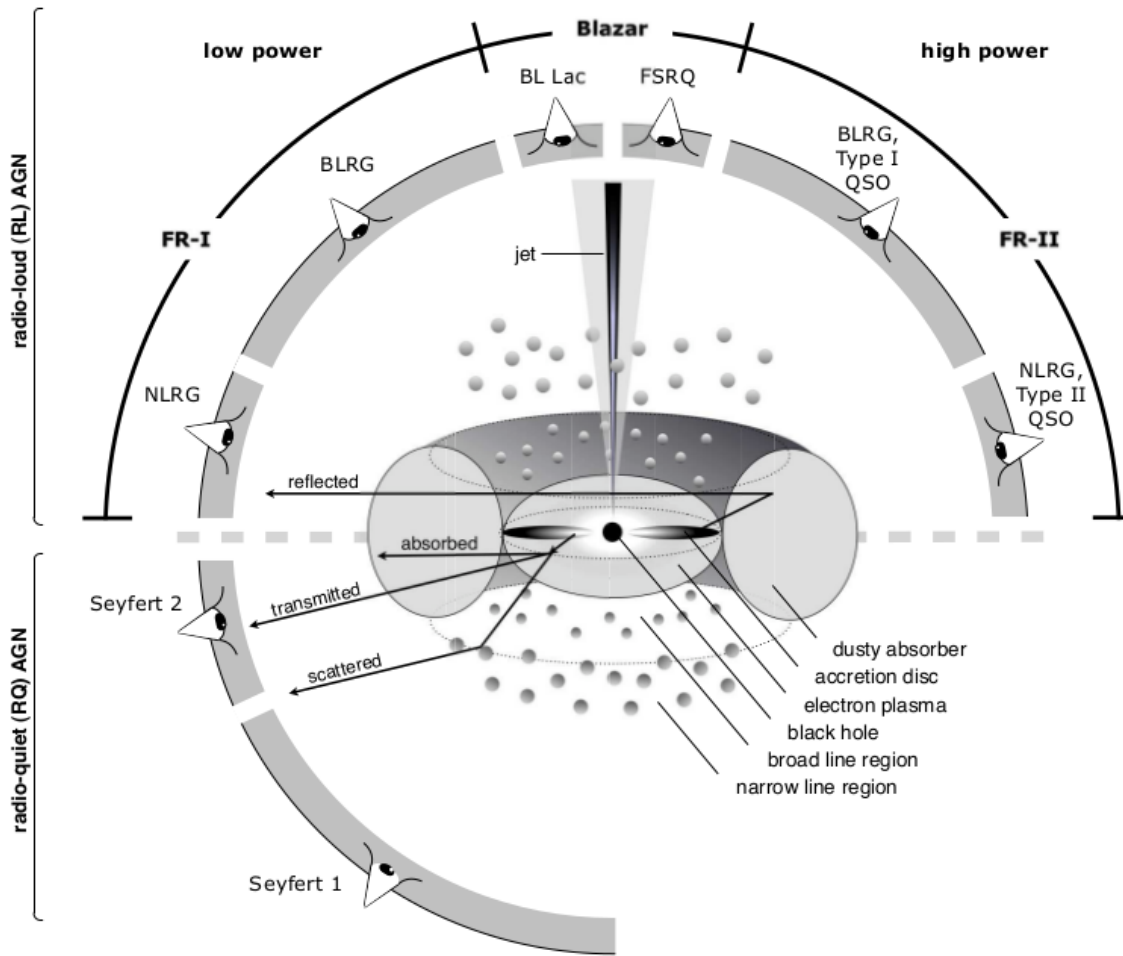


Figure 1.1: Unification model for radio-loud and radio-quiet AGN (Beckmann & Shrader 2012). The scheme shows the different types of AGN depending on the orientation, presence or absence of the jet, and accretion power.

The radio-quiet AGN have a relatively weak emission in radio and are classified at low-luminosity as Seyfert galaxies, and at high luminosity as quasars. Seyfert galaxies are further classified by their optical emission lines as Seyfert 1 (Sy1) and Seyfert 2 (Sy2) galaxies. Sy1 galaxies present narrow and broad lines in their spectra, since we see the AGN more pole-on and we have a direct view of the BLR and NLR. Sy2 galaxies present only narrow lines in their spectra, since we see the AGN edge-on and the accretion disk, corona and BLR are partially or fully obscured by the torus.

Figure 1.1 shows a unification scheme that pulls together our understanding of the various AGN phenomenon, representing the different types of AGN depending on the orientation, radio loudness and accretion.

1.3 X-ray emission in AGN and the Fe $K\alpha$ line

The primary X-ray emission is modeled by a power-law. The flux of the continuum as a function of the photon energy is given by:

$$F(E) = k \cdot E^{-\Gamma} \text{ photons cm}^{-2} \text{ s}^{-1} \text{ keV}^{-1}, \quad (1.2)$$

where k is the normalization at 1 keV and Γ is the photon index.

The X-ray emission can be affected by absorption from circumnuclear matter through two processes: photoelectric absorption (bound-bound and bound-free transitions) and Compton scattering. The absorption processes lead to the depletion of the X-ray continuum preferentially at lower energies (since absorption cross section goes as $\approx E^{-3}$), with higher column densities leading to stronger absorption and up to higher energies.

A bound-bound transition occurs when an atom absorbs a photon, increasing the energy of a bound electron. The electron changes its energy level from E_i to a higher energy level E_j . To get back to its original state, the electron emits a photon with energy $E = h\nu = E_j - E_i$, with some broadening due to quantum mechanical and macroscopic (e.g., doppler) effects.

A bound-free transition occurs when an atom absorbs a photon, imparting sufficient energy (i.e. greater than the ionization potential) to a bound electron to liberate it to a free state, leaving behind an ion. This process is also known as photoionization. The inverse process is called recombination, which occurs when an ion captures a free electron and emits one or more photons.

Compton scattering occurs when a photon hits a free or a bound electron (in a neutral atom). In the first case, if the energy of the photon is much less than the rest mass energy of the electron, $h\nu_0 \ll m_e c^2$, the process is described by the Thomson scattering. This is an elastic process in which the particle absorbs the photon, is set into motion and then re-emits a photon with the same energy. In the second case, when the interaction is with a neutral atom, the target electron is ionized through the scattering. The process is affected by the binding, therefore the final energy of the electron will depend in the momentum of the atomic system.

On the other hand, when the photon energy is comparable with the rest mass energy of the electron, quantum effects become important, since the photon carries momentum as well as energy. In this case, energy will be transferred from the photon to the electron, leading to a recoil in the

electron and a loss of the photon energy. The change of the photon energy is $\Delta E = h(\nu_f - \nu_i)$, where the subindices f and i correspond to the final and initial frequency, respectively.

One of the most important characteristics in the X-ray spectra of AGN is the so-called reflection component, which is produced by the combination of bound-free absorption and Compton scattering of the primary emission, from very dense circumnuclear matter (torus component). The quantity of reflected photons depends on the hydrogen column density of the matter (N_H) and its covering factor, which is the fraction of the sky covered by dust and gas.

We can observe neutral reflection in the AGN spectra through two important features: the Fe $K\alpha$ fluorescence line at 6.4 keV and the Compton hump around 30 keV. The Fe $K\alpha$ line is produced when an electron of an iron atom K-shell is ejected after photoelectric absorption of a high energy X-ray photon ($E > 10$ keV). Then, an excited state electron decays, emitting a 6.4 keV photon. The Compton hump arises from the Compton scattering process of high energy photons too. Both features are thought to originate from the broad line-emitting (BLR) and torus regions. Figure 1.2 shows the X-ray spectra of an obscured AGN, where the Fe $K\alpha$ line and the Compton hump (Reflection hump in the figure) are depicted. At high column densities ($N_H \gtrsim 10^{24} \text{ cm}^{-2}$) the transmitted power-law is depleted, and these two features become more prominent.

The Fe $K\alpha$ line is composed of a broad component plus a narrow core. The broad part is thought to be produced by material near enough to the SMBH to be affected by Doppler and gravitational broadening (e.g., Mushotzky et al. 1995; Tanaka et al. 1995; Yaqoob et al. 1995). Reverberation studies suggest that the broad line originates from a compact zone near to the SMBH, with only a few r_g of extension (e.g., Cackett et al. 2014). On the other hand, the narrow component probably originates on parsec scales, in the dusty torus (e.g., Ghisellini et al. 1994; Krolik et al. 1994; Yaqoob et al. 1995).

1.4 Motivation and goals

X-ray continuum and Fe $K\alpha$ line variability is commonly observed in all obscured, and even some heavily obscured AGN (e.g., Yaqoob et al. 1996; Iwasawa et al. 1996; Lamer et al. 2003; Zoghbi et al. 2019; Marinucci et al. 2018; Ponti et al. 2013). Through variability timescales we can understand the emission mechanisms in AGN and probe the inner regions, within a few r_g from the

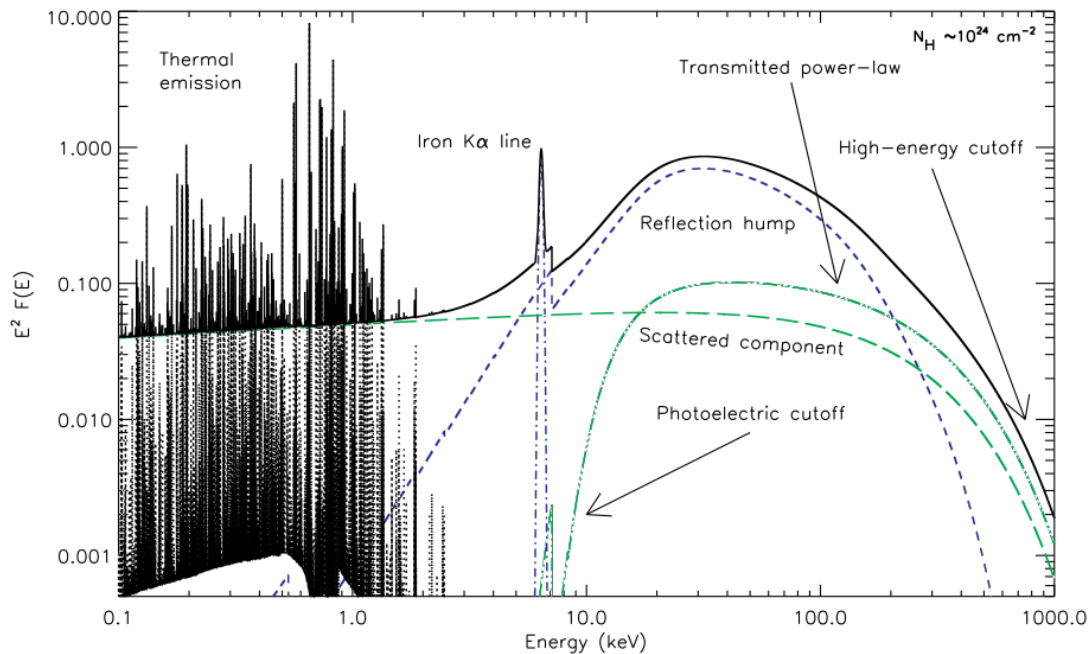


Figure 1.2: AGN spectra with a $N_H \sim 10^{24} \text{ cm}^{-2}$. Several important X-ray features are depicted, such as the thermal emission (not mentioned in this work), the Fe $K\alpha$ line, the Reflection hump (or Compton hump), the transmitted power-law and the scattered component. The relative normalizations in this figure are illustrative only. Figure courtesy of Claudio Ricci.

black hole. In particular, some studies have constrained the location and size of the Fe $K\alpha$ emitting region by studying the reaction of the Fe $K\alpha$ line to continuum variations (e.g., Ponti et al. 2013; Zoghbi et al. 2019).

An interesting behaviour for the Fe $K\alpha$ line was observed in MCG-6-30-015 by Iwasawa et al. (1996), using a 4-day observation performed by the ASCA observatory (Tanaka et al. 1994), with the Solid-state Imaging Spectrometer (SIS) in Faint/ICCD mode and the Gas Imaging Spectrometer (GIS) in PH mode. They performed a double Gaussian fit to analyse separately the broad and narrow components of the Fe $K\alpha$ line. Their results are briefly discussed next.

Figure 1.3 shows the comparisons between the intensity and equivalent width (EW) of the narrow and broad components of the line, and the 3-10 keV continuum. They found a positive correlation between the intensity of the narrow component of the line and the continuum (top panel). This suggests that the narrow component is near enough to the X-ray corona to react to continuum variations in less than 4 days, which corresponds to light crossing sizes comparable to

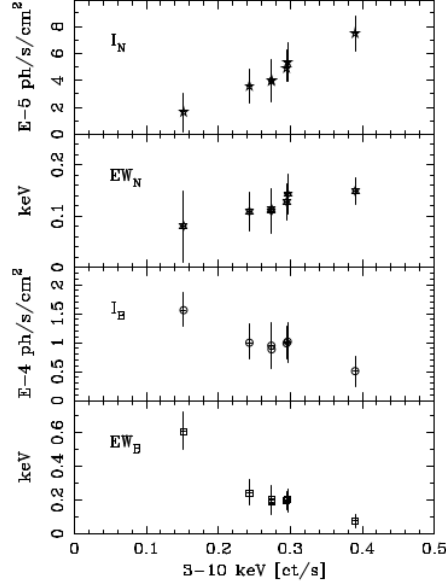


Figure 1.3: Figure reproduced from Iwasawa et al. (1996), showing the 3-10 keV count rate versus the intensity of the narrow component of the Fe $K\alpha$ line (first panel), the EW of the narrow component of the Fe $K\alpha$ line (second panel), the intensity of the broad component of the Fe $K\alpha$ line (third panel) and the EW of the broad component of the Fe $K\alpha$ line (fourth panel).

the accretion disk or innermost BLR clouds. The result is surprising since at that distance from the central SMBH the line should be broadened by gravitational effects. Moreover, they found a slight anti-correlation between the intensity of the broad component and the continuum (third panel). In the paper, the authors recognize that this behaviour is difficult to understand and they discuss different implications that could affect it. These results indicate that the narrow component of the line reacts faster than the broad component to the continuum variation, though varying in a manner opposite to expectations.

The second and bottom panels of the Figure 1.3 show comparisons between the EW of the narrow and broad components of the line and the continuum, respectively. The EW of the narrow component is about constant while the EW of the broad component anti-correlates with the continuum. The previous results support that the line is originated in different regions.

While spectral investigations can place important constraints on reflection close to a SMBH, there are a number of studies based on observations from the *Chandra* X-ray observatory, which have found Fe $K\alpha$ emission extending out hundreds to thousands of light years for the galaxies NGC 4151 (Wang et al. 2011), NGC 6240 (Wang et al. 2014) and NGC 4945 (Marinucci et al. 2017).

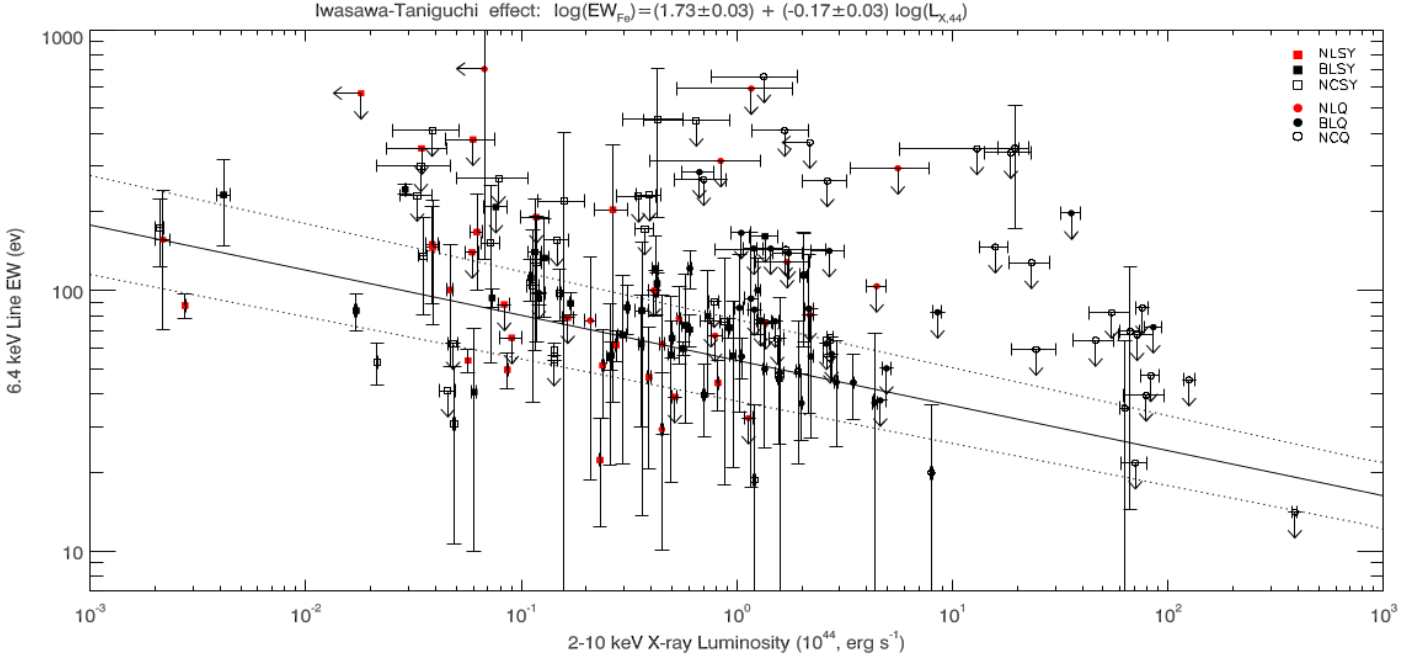


Figure 1.4: Figure from Bianchi et al. (2007). The IT effect: Fe $K\alpha$ line EW against 2–10 keV X-ray luminosity for 157 radio-quiet Type 1 AGN. The different symbols refer to the classification of the objects, based on their absolute magnitude and $H\beta$ FWHM: NLSY, narrow-line Seyfert 1; BLSY, broad-line Seyfert 1; NCSY, not-classified Seyfert 1 (no $H\beta$ FWHM measure available); NLQ, narrow-line quasar; BLQ, broad-line quasar; NCQ, not-classified quasar (no $H\beta$ FWHM measure available). The analytical expression for the best fit line is reported on the top.

These scales are much larger than putative sizes of the dusty torus, which several ALMA studies have proved to be $\lesssim 10$ pc (e.g., Gallimore et al. 2016; Imanishi et al. 2016; García-Burillo et al. 2016).

Another result supporting the fact that the Fe $K\alpha$ emission could be extended is the X-ray Baldwin effect, also known as the Iwasawa-Taniguchi (IT) effect, which describes the anti-correlation between the EW of the Fe $K\alpha$ line and the 2–10 keV continuum. Bianchi et al. (2007) studied this effect in radio-quiet AGN, as main result the trend shown in Fig. 1.4. The IT effect is accounted by variability effects, assuming that the Fe $K\alpha$ originates at larger scales and the line does not suffer significant fluctuations within timescales of months to years. Therefore, the EW of the narrow line would be naturally smaller while the continuum is in a higher state (Jiang et al. 2006).

The goal of our work is to try to understand the structure of the reflecting clouds in AGN, what

fraction of the Fe $K\alpha$ emission is produced very close to the nucleus, and study to what extent this fraction varies among a large AGN sample. Does this fraction show any relation with AGN and host galaxy properties such as the SMBH mass, the equatorial column density, the accretion rate, the AGN type, galaxy type, morphology, or gas content? To answer these questions we performed an spectral and imaging analysis using observations of *Chandra* and *XMM-Newton*, studying the reaction of the narrow Fe $K\alpha$ line to continuum variations and the spatial extension of the Fe $K\alpha$ emission.

Chapter 2

Data analysis

In this chapter, we describe the observations used to analyze the Fe $K\alpha$ line variability, the data reduction and spectral extraction, the spectral fitting and creation of the light curves, and lastly, the imaging analysis.

2.1 Observations and data reduction

2.1.1 Sample selection

Our parent sample is the most-recent 105-month *Swift* - Burst Alert Telescope (BAT) Survey (Oh et al. 2018), an all-sky survey in the ultra-hard X-ray band (14–195 keV), which provide an unbiased AGN sample to highly obscured AGN ($N_{\text{H}} > 10^{24} \text{ cm}^{-2}$) (Ricci et al. 2015). We carried out this research with observations from *Chandra* (Weisskopf et al. 2000) and *XMM-Newton* (Jansen et al. 2001) due to their high sensitivity in the 2–10 keV band of $\sim 10^{-15} \text{ erg s}^{-1} \text{ cm}^{-2}$ (Hasinger et al. 2001), good spectral resolution and high *Chandra* resolution images. We further complemented this sample with some additional local AGN from the subarcsecond-resolution mid-infrared (MIR) atlas of Asmus et al. (2014). The 105-month *Swift*-BAT catalog is a uniform hard X-ray all-sky survey with a sensitivity of $8.40 \times 10^{-12} \text{ erg s}^{-1} \text{ cm}^{-2}$ over 90% of the sky in the 14–195 keV band. The survey provides 1632 hard X-ray sources and at least 947 of them are AGN. The MIR atlas is comprised of 253 AGN in the local universe (median redshift of $z = 0.016$); the majority of the

¹<https://cxc.harvard.edu/proposer/POG/html/ACIS.html>

sources are in the 9-month BAT catalog (Winter et al. 2009), but it adds an interesting subset of additional local AGN with imaging observations available from any high angular resolution MIR instrument with a public archive.

We applied a flux cut in $F_{14-195 \text{ keV}} \geq 10^{-11} \text{ erg s}^{-1} \text{ cm}^{-2}$ and $F_{0.5-7 \text{ keV}} \geq 3 \times 10^{-13} \text{ erg s}^{-1} \text{ cm}^{-2}$; these limits yield what we consider to be the bare minimum in terms of photon statistics (~ 250 counts in a 10ks observation) to enable spectroscopic constraints from typical observations ($\geq 10-20$ ks). For example, we might expect between 1–5% of the photons detected by *Chandra* or *XMM-Newton* to arise from Fe $K\alpha$ in a typical AGN; thus 250 total counts equates to 3-15 counts in the line. This resulted in the selection of 252 sources in the local universe ($z < 0.1$), and 28 more distant galaxies with redshifts between 0.1 and 0.56.

In the next subsections, we describe the observations and data reduction for each observatory.

2.1.2 *Chandra* X-ray Observatory

We downloaded all the data available in the *Chandra* archive associated with source in our sample, obtaining 1001 observations. We chose data observed with the Advanced CCD Imaging Spectrometer (ACIS) in both CCD configurations (ACIS-S and ACIS-I), but not from the High Resolution Camera due to the much lower spectral resolution. 279 of the 1001 observations were acquired in the High-Energy Transmission Grating mode ((Canizares et al. 2000), HETG). The HETG is comprised of two grating assemblies: the High Energy Grating (HEG, 0.8–10 keV) and the Medium Energy Grating (MEG, 0.4–5 keV); we only used the HEG spectra, since our focus was on the study of the 2–10 keV spectra, and in particular the region around the 6.4 keV Fe $K\alpha$ line to make our analysis. The observations were acquired between years 2000 to 2018.

Figure 2.1 shows a HETG observation. The top panel depicts the zeroth-order image (similar to a normal ACIS observation, but with lower high-energy sensitivity) in the CCD S3 and an X-shaped feature, which represents the dispersed HEG and MEG spectra (or first-order and second-order spectra). Each grating disperses the photons with an offset of 10° , forming the X-pattern. The lower three panels show zoom-in views of the MEG –1-order spectrum, where the numbers are the wavelength of the emission lines in the spectra, in Angstrom units.

The raw data are event files; an array which stores the information about energy, position and time for each event. The event file contains photon event data stored as a table, Good Time

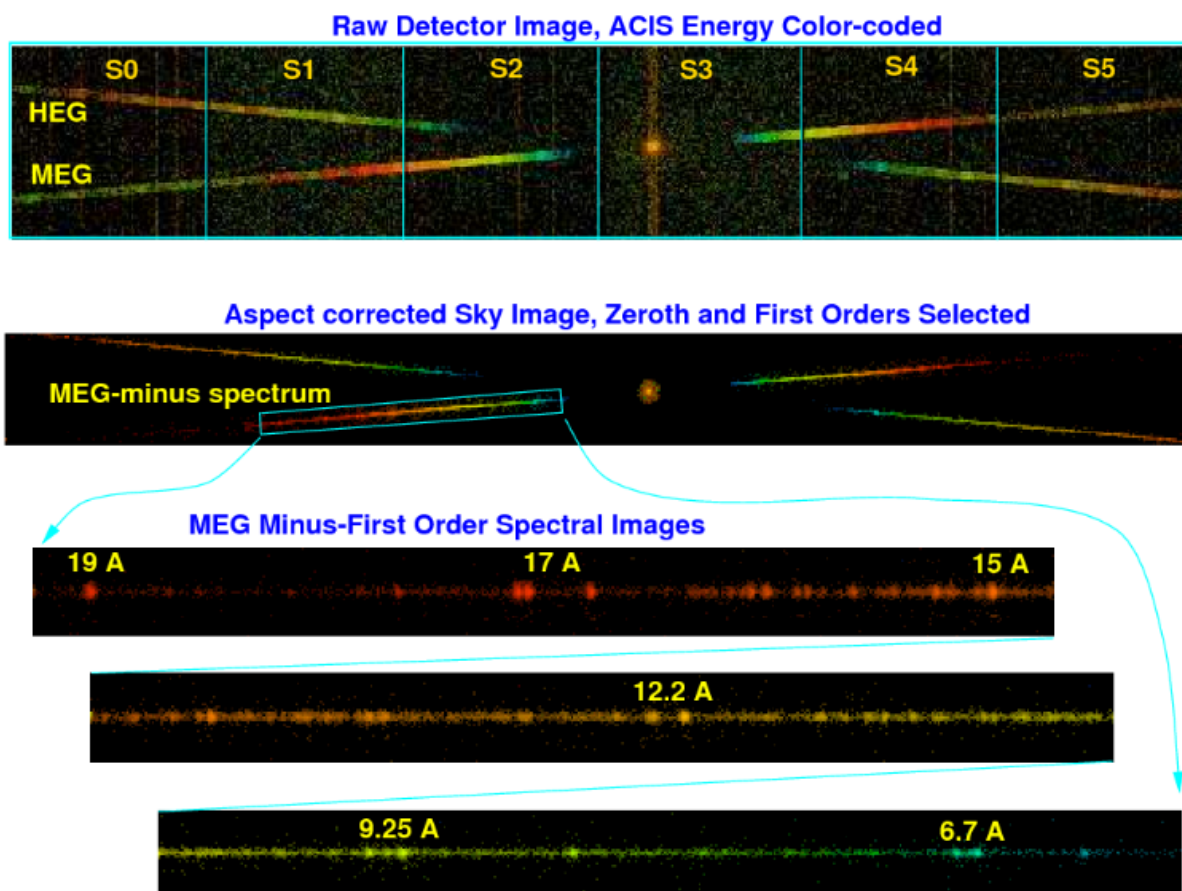


Figure 2.1: HETG observation of Capella, ObsID 1318, obtained from Chapter 8 of the *Chandra* Proposer’s Observatory Guide, Cycle 22. The top panel shows the raw zeroth-order image (similar to a normal ACIS observation) in the CCD S3 and an X-shaped feature, which is the dispersed HEG and MEG spectra (first-order and second-order spectra). The second panel shows an aspect corrected image after selection applied only to include the zeroth and first-order events. The last three panels show zoom-in views of the MEG –1-order spectrum, where the numbers are the wavelengths of the emission lines in the spectra, in Angstrom units.

Intervals, weight map, etc. We made the data reduction following the standard procedure with the CIAO software (v 4.11) and calibration files (CALDB v 4.8.3), using the `chandra_repro` script. Since the galaxy centers in the images were slightly shifted from the real position of the galaxies in some observations, we manually chose the center of each observation and made the alignment, creating a new aspect solution using the `wcs_update` task. We had to make the alignment manually for two reasons. First, in some observations, there were not enough point sources in the field in common to match and align them automatically, and second, in several observations the saturation was very high, producing a hole in the center of the source which confused the alignment code (see Fig. 2.2). After creating the new aspect solution, we removed background flares from the event files with the script `deflare` and we subtracted the readout streak, with the `acisreadcorr` task, to be more precise in the spectral and imaging analysis. The readout streak is a line that passes through the source composed of photons detected during the readout time. When the source is very bright, the readout streak is bright too. An example of this is shown in Figure 2.2. Finally, we reprojected the events using the `reproject_events` task to make a proper imaging analysis.

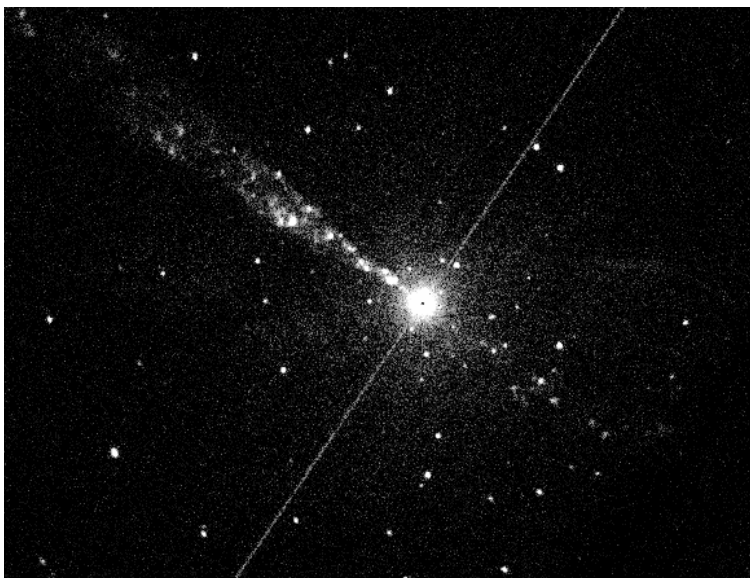


Figure 2.2: ACIS observation of the galaxy Centaurus A Obsid 20794. The thin diagonal line crossing the source is the readout streak. The observation is very affected by saturation, producing a hole in the center of the image. We can also see off-nuclear X-ray sources associated with the galaxy and background AGN, as well as a clumpy jet; we must take care to avoid these features for some analyses.

For regular ACIS observations and Oth-order HETG, we extracted the spectra with the `specextract`

task, which creates the spectra and the responses files (ARF and RMF). We generated spectra for a 1.5'' radius circular aperture and an annulus of 3''–5'' for each observation, using an annular background region of 20''–35'' aperture. We removed all the off-axis point sources in the field before the extraction. We used the circular spectra for the observations unaffected by saturation and the annular spectra for the rest (see section 2.2.2). We applied an aperture correction to the 1.5'' circular spectrum and the annular spectra using the `arfcorr` task, creating proper responses files.

For the HETG observations, we extracted the 1st-order dispersed spectra using a 6-pixel width aperture. We first made a mask to find HEG and MEG arms, using the `tg_create_mask` task, and then we resolved the spectral orders using the `tg_resolve_events` task. Lastly, we created the spectra and the response files using `tgextract` and `mktgresp`, respectively.

2.1.3 *XMM-Newton*

To complement the *Chandra* data, we added 90 observations performed by the CCD camera EPIC-pn of *XMM-Newton*, provided by Alessia Tortosa. She is aiming to study the spectral variability for the unobscured Type 1 AGN of the BASS sample, and therefore her sample comprise only a subset of our sample. She is currently working on the data reduction, hence we only used part of the total available *XMM-Newton* data for this work.

The EPIC cameras offer sensitive imaging between 0.3–12 keV, with a spectral resolution of $E/\Delta E \sim 30\text{--}50$. The full frame time of the pn camera is 73.3ms per CCD (Jansen et al. 2001). Due to the low frame time, the spectra are not affected by saturation.

The *XMM-Newton* spectra were reduced and extracted by Alessia with SAS (v 1.3). The extraction radius is optimized to have the best signal to noise for each observation, therefore it is not always the same, ranging between 20'' and 40''. The spectra are aperture corrected.

To properly compare the fluxes obtained from the different instruments, we multiplied the fluxes obtained from the pn/*XMM-Newton* spectra by a cross calibration constant. Madsen et al. (2017) found that the fluxes measured from the HEG spectra are 1.17 times greater than the pn spectra; we adopted this constant.

2.2 Spectral analysis

The goal of the spectral analysis is to study the variability of the Fe $K\alpha$ line and continuum fluxes between observations, hence we need at least two observations per source. 121/280 sources have only 1 observation, therefore the sample is reduced to 159 sources.

To study the Fe $K\alpha$ line reaction to continuum variation, we performed a spectral fitting for each observation and constructed light curves from the best-fitting Fe $K\alpha$ line and 2–10 keV continuum fluxes for each source. We explain below how we computed the fluxes and analyzed the light curves.

2.2.1 Spectral fitting

We fit the spectra using the python package PyXspec², which is based on the popular standalone X-ray spectral fitting package XSPEC (version 12.10.1, (Arnaud 1996)). We applied a simple model to compute the fluxes of the Fe $K\alpha$ line and the continuum between 2–10 keV, given by

$$\text{PHABS_1} \times \text{PHABS_2} \times (\text{CPFLUX_1} \times \text{POWERLAW} + \text{CPFLUX_2} \times \text{ZGAUSS}) \quad (2.1)$$

where the `PHABS_1` and `PHABS_2` components account for the Galactic and intrinsic AGN line-of-sight absorption, respectively, the `POWERLAW` component corresponds to the continuum emission, and the `ZGAUSS` term reproduces the Fe $K\alpha$ line emission at 6.4 keV. The `CPFLUX_1` and `CPFLUX_2` components provide the photon fluxes of the continuum emission and the Fe $K\alpha$ line, respectively. Figure 2.3 shows an example of the fit for an observation of Centaurus A. The model reproduces fairly good the 2–10 keV spectra, which is strongly attenuated by absorption and present a notorious emission line at 6.4 keV.

2.2.2 The pileup problem and its solution

Saturation, or more precisely photon "pileup", occurs when two or more photons fall in the same pixel within a single exposure "frame" and, in consequence, the information in that pixel is altered. If the source is very bright or the frame time is high, there is a higher probability to be affected

²<https://heasarc.gsfc.nasa.gov/docs/xanadu/xspec/python/html/index.html>

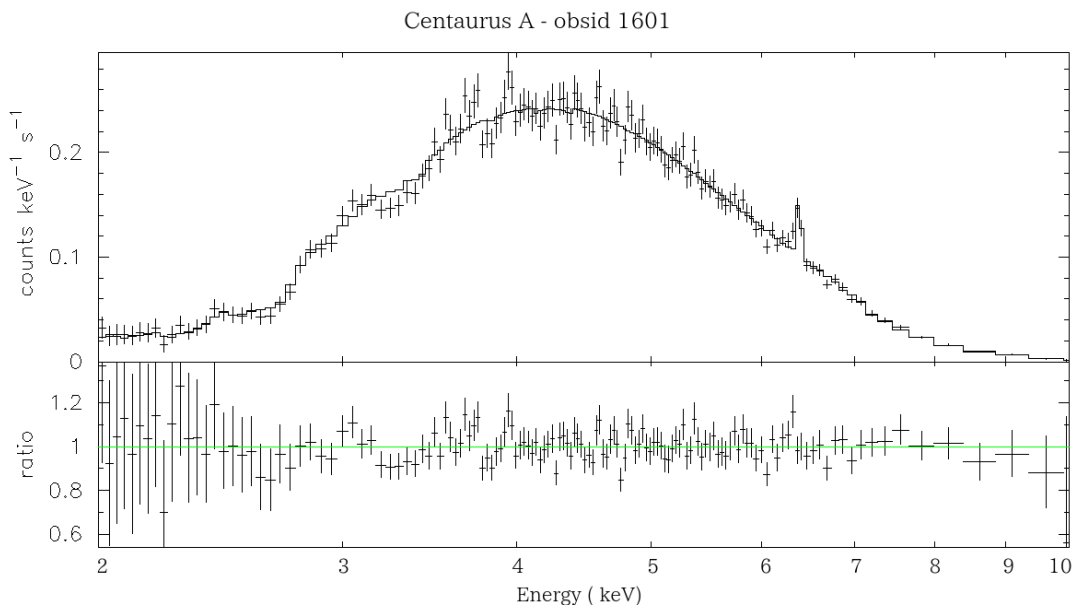


Figure 2.3: 2–10 keV spectrum for the Type 2 AGN Centaurus A, obsid 1601, fitted by the model described in Eq.2.1. The spectrum is attenuated by the strong absorption. The unique notorious emission line is the Fe $K\alpha$ line at 6.4 keV.

by saturation. Figure 2.2 shows an observation of Centaurus A, where the high amount of pileup produces a hole in the center of the image.

Normal CCD observations with the ACIS camera of *Chandra* are commonly affected by pileup since the nominal frame time of the camera is 3.2 seconds, enough time to suffer saturation. The *Chandra* grating spectra are less affected by pileup since a large fraction of the photons are dispersed to the 1st and 2nd orders instead of the 0th order. The *XMM-Newton* pn observations are also less affected by pileup due to the much smaller frame time of that instrument (see section 2.1.3).

We cannot use saturation-affected data to study flux variability, and thus we need to know whether each ACIS observation is affected by pileup. A good way to estimate the amount of pileup of an observation is to compute the count rate per frame time of the observation, since it has a relation with the pileup fraction³. When the count rate per frame is less than 0.1, the pileup fraction is < 5%. We used this threshold to separate saturated from unsaturated observations.

To compute the real count rate per frame time of each observation, we used the 3''–5'' annular spectra for all the ACIS observations, and the following expression:

³https://cxc.harvard.edu/csc/memos/files/Davis_pileup.pdf

$$\text{count rate per sec}_{3''-5''} \times (100/3) \times \text{frame time} \quad (2.2)$$

The factor (100/3) is explained by Figure 2.4, obtained from the *Chandra* Proposer’s Observatory Guide⁴. The fractional power encircled in a 3’’–5’’ annulus is around 3% of the total power, and therefore we need to correct the count rate per second of the annular spectra by the inverse of this value (i.e., applying an aperture correction).

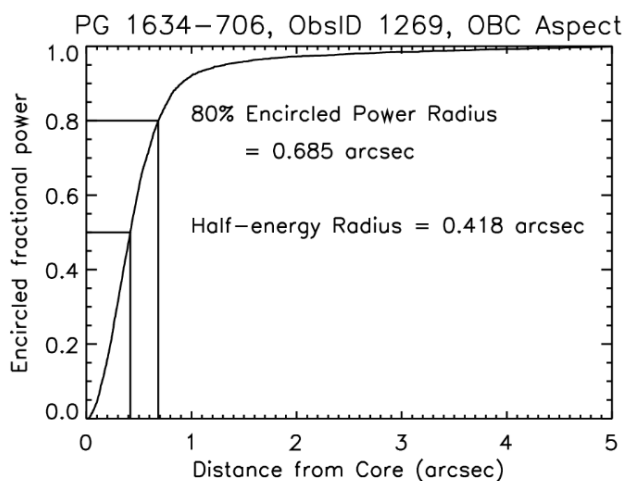


Figure 2.4: Example of the encircled energy at 1 keV versus circular extraction aperture radius for ACIS observation of the point source PG1634-706 (ObsID 1269). The encircled energy depends on the energy and off-axis angle.

If the observation is affected by pileup, we adopted the aperture-corrected 3’’–5’’ annular spectrum, if not, we used the aperture-corrected 1.5’’ circular spectrum.

We discovered an inconsistency when comparing fluxes given by the 1.5’’ aperture and 3’’–5’’ annular spectra, suggesting that the aperture correction in the annular spectrum fails. Given that the central aperture spectra could be affected by saturation, we performed a consistency check between the 3’’–5’’ annular spectrum with the HEG spectrum in the 2-10 keV energy range, for all the observations performed in normal and grating mode. To do this, we used PyXspec to fit the following simple model:

$$\text{CONSTANT} \times \text{PHABS_1} \times \text{PHABS_2} \times (\text{POWERLAW} + \text{ZGAUSS}) \quad (2.3)$$

⁴<https://asc.harvard.edu/proposer/POG/html/chap6.html>

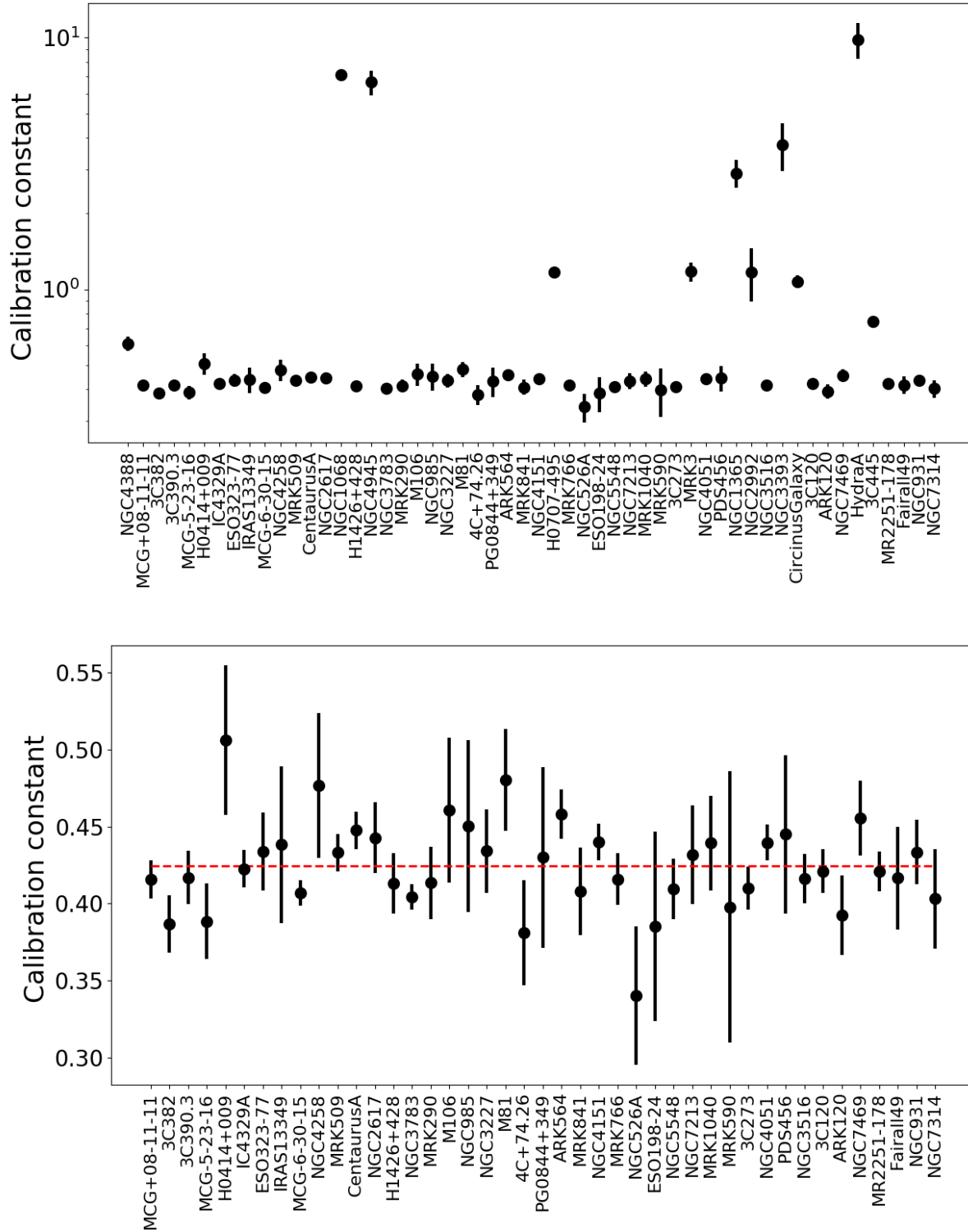


Figure 2.5: Calibration constants between the *Chandra* HEG 1st order and ACIS/HETG 0th order 3''–5'' annular spectra. The upper panel shows all the calibration constants, and the lower panel shows the calibration constants consistent with the "floor" found at 0.424 ± 0.00507 , marked by a red dashed line.

The description of each component is the same that in Section 2.2.1, with the exception of the CONSTANT component, which was added to compute the calibration constant between the spectra. The constant value was fixed to 1 for the grating spectrum and let free to vary for the annular spectrum.

The upper panel of Figure 2.5 shows the calibration constants calculated for the sample. We obtained an evident consistency for 43/53 galaxies. For the rest of the sources, higher values for the calibration constant were computed, therefore we did not use the 3''–5'' annular spectra for those cases. A possible explanation for the outlier sources may be extended emission. Some of the sources with a constant higher than one are already claimed to present extended emission, such as the Circinus Galaxy (Arévalo et al. 2014), NGC 1068 (Bauer et al. 2015) and NGC 4945 (Marinucci et al. 2017). We should make an analysis of the rest of the sources to confirm this theory, but for now this is the most probable explanation.

Lower panel of Figure 2.5 shows the values of the calibration constants consistent between them. The average value for the constant is 0.424 ± 0.00507 , which is highly constrained and we used it to re-scale the fluxes obtained from the annular spectra, to compare them with the fluxes obtained from the non-pileup spectra. If the aperture correction was accurate, we would expect a constant consistent with one. The corrections are based on simulations of the *Chandra* point spread function (PSF), hence the value of the constant claims for a problem with the simulations. We found information in the *Chandra* website about a inconsistency between theoretical and real PSF⁵, confirming our suspicions. We had to deal with this problem when we made the analysis of the *Chandra* images. We present the PSF caveats in more detail in Section 4.1.

2.2.3 Light curves analysis

To assess whether the light curve are variable or not, we used the parameter P_{var} (e.g, Paolillo et al. 2004; Lanzuisi et al. 2014; Sánchez et al. 2017), which computes the probability $P_{var} = P(\chi^2)$ that a χ^2 lower than the observed could occur by chance, for a non-variable source. The expression for the chi-squared (χ^2) score is:

⁵<https://cxc.cfa.harvard.edu/ciao/PSFs/chart2/caveats.html>

$$\chi^2 = \sum_{i=1}^{N_{obs}} \frac{(x_i - \bar{x})^2}{\sigma_{err,i}^2} \quad (2.4)$$

where N_{obs} is the number of observations, x_i is the flux measured at each observation, \bar{x} is the mean flux per light curve, and $\sigma_{err,i}$ is the flux error. If a source is not variable, we expect that $\chi^2 \sim N_{obs} - 1$. The typical threshold to distinguish variable from non-variable light curves is $P_{var} = 0.95$ (e.g., Paolillo et al. 2004; Papadakis et al. 2008), which indicates a 95% of probability that the source is intrinsically variable.

2.3 Imaging analysis

To complement the spectral analysis, we studied the high resolution *Chandra* images to see whether some sources are spatially extended and conciliate it with the spectral results. We carried out the imaging analysis using radial profiles. For each source, we merged all the event files with an off-axis angle $< 2'$ (to avoid observations affected by strong distortions to the PSF), using the task `reproject_obs`. This task reprojects the observations to a common tangent point and then merges them. We excluded photons related to the 1st-order spectrum (when the observations were made in grating mode) and off-nuclear point sources in the field. Then, we extracted radial profiles for each source with `dmextract`, using sequential annuli. After removing the 1st-order spectrum and the point sources, we account for the removed area from each annulus.

Figure 2.6 shows an example an merged image for Circinus Galaxy, before and after removing the off-axis point sources. The green circles represent the annular regions selected to extract the radial profiles.

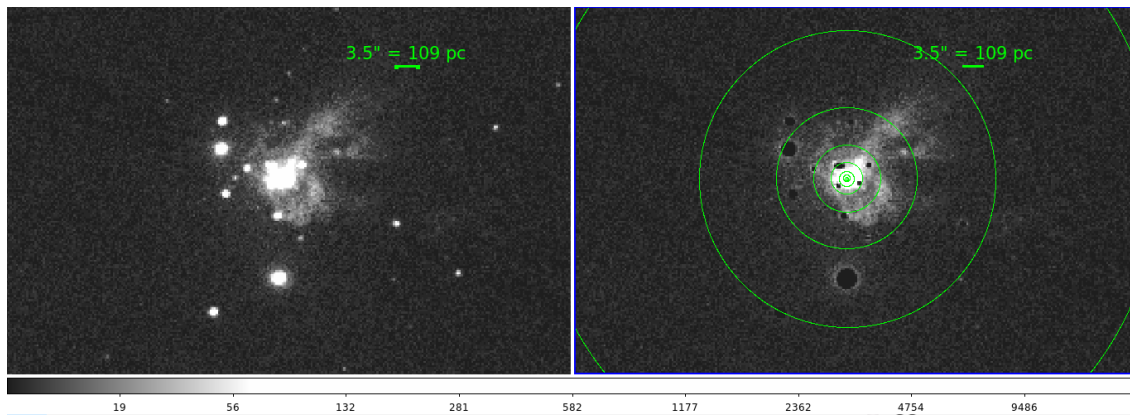


Figure 2.6: Merged image of all the ACIS observation available for Circinus Galaxy. The right image is the original, and the left image is after removing all the point sources. The green circles represent the annular regions used for the radial profiles extraction, using a logarithmic binning.

Chapter 3

Chandra and *XMM-Newton* spectral results

We started our analysis by fitting the spectra of all the observations and studying whether there is a reaction of the Fe $K\alpha$ line to the 2–10 keV continuum variations for different sources. In this section we present the dependence of the Fe $K\alpha$ line emission with the continuum emission for our sample, its (non)correlations with AGN and host galaxy properties, and the problems we had to constrain the line - continuum flux relation.

3.1 Fe $K\alpha$ line and 2–10 keV continuum behavior

We assembled light curves for the fluxes of Fe $K\alpha$ line ($F_{6.4\text{ keV}}$) and the continuum between 2–10 keV ($F_{2-10\text{ keV}}$) for all our sources, and analyzed them statistically to understand how the line reacts to continuum variation.

To assess if the fluxes of the Fe $K\alpha$ line and the continuum are related, we fit a first-order polynomial using the python package Linmix. This package is based on the code of Kelly (2007), which describes a Bayesian method to account for measurement errors of astronomical data. We chose this code since it does not assume a particular distribution for the errors and incorporates non-detections, both of which are fundamental for this study since in several cases the fluxes of the Fe $K\alpha$ line are upper limits. The flux errors obtained in XSPEC are mildly asymmetric, however we symmetrized them in order to use them as input in Linmix.

The Linmix package requires at least 5 measurements, and therefore, all the sources with 4 or fewer observations cannot be analyzed statistically using this method. This reduces our sample

from 159 to 38 galaxies, since the vast majority have only 2-3 observations, and some *Chandra* observations with pileup spectra with an inconsistent calibration constant had to be discarded (see Section 2.2.2). The linear regression fit resulted in 19 AGN with well-constrained slopes and 19 AGN with slopes not constrained at all. Figure 3.1 shows the comparison between the Fe $K\alpha$ line and continuum fluxes for the sources with well-constrained slope and Table 3.1 shows the values of the well-constrained slopes, the maximum light curve timespan, the P_{var} parameters obtained for the Fe $K\alpha$ line and 2–10 keV continuum light curves, and whether the sources are radio-loud or radio-quiet AGN. Section 3.2 presents an analysis of the problems that we had to constrain the slopes.

Figure 3.2 shows the $F_{6.4\text{ keV}}-F_{2-10\text{ keV}}$ slopes for all sources, demonstrating we found a wide variety of behaviors, which can be separated in 3 cases. For the first case, the Fe $K\alpha$ line flux is dominated by emitting clouds located in a compact zone, near to the X-ray corona, therefore the line flux reacts quickly to the continuum variations on timescales comparable to the observation exposure, obtaining a slope near or consistent with one for 8 sources. The reaction of the reflecting clouds could be from light-days to light-years, suggesting that for those sources the Fe $K\alpha$ line originates in the accretion disk, the BLR and/or inner walls of the torus. For some of these sources, P_{var} indicates that the Fe $K\alpha$ emission is not variable, but we still consider the slopes to be robustly determined, because we see correlated variability behavior between the two fluxes. For the second case, the line flux is dominated by clouds located at larger scales, in an extended region, and the line flux does not react to continuum variation in the observations timescales, obtaining a $P_{var} < 95\%$ and a $F_{6.4\text{ keV}}-F_{2-10\text{ keV}}$ slope near or consistent with zero, suggesting perhaps that the reflecting clouds may be located in an extended region (i.e., torus scales), much more distant from the X-ray corona (more complex scenarios may also be possible). For the third case, there are sources in where both the continuum and Fe $K\alpha$ line fluxes vary, but they do not correlate, suggesting a more complex picture (perhaps related to a specific geometry, spectral complexity, and/or timescales of X-ray continuum variability which are much shorter than the light travel time to the X-ray reflector).

Next, we illustrate 3 common behaviors repeated in our sample. A good example is the Centaurus A AGN. Figure 3.3 presents the light curves for the 2–10 keV continuum and Fe $K\alpha$ line fluxes for this AGN, constructed with *Chandra* observations, spanning 18 years, in normal and grating mode. We found a variation of almost two orders of magnitude for both the continuum and Fe $K\alpha$ fluxes.

Source	slope	lc timespan (years)	P_{var} Fe $K\alpha$ lc	P_{var} continuum lc	Radio-loud AGN
3C273**	0.59 ± 1.45	17.06	0.73	1	yes
Centaurus A**	1.05 ± 0.19	18.03	1	1	yes
Circinus Galaxy	-0.29 ± 0.7	8.72	0.98	0.99	no
Cygnus A	1.24 ± 0.68	17.01	1	1	yes
IC4329A	1.24 ± 0.27	17.04	1	1	no
M51a	0.83 ± 0.78	17.15	0.26	1	no
M81	0.87 ± 0.33	16.86	0.99	1	yes
MCG-6-30-15	0.37 ± 0.62	12.57	1	1	no
MRK290	0.038 ± 0.89	2.85	0.31	1	no
MRK509	0.32 ± 0.24	11.87	0.87	1	no
NGC3516	0.18 ± 0.32	6.04	0.83	1	no
NGC3783	0.15 ± 0.28	16.6	0.4	1	no
NGC4051	0.18 ± 0.26	16.07	0.99	1	no
NGC4151	-0.14 ± 0.38	14.01	1	1	no
PictorA*	0.7 ± 0.3	14.98	0.82	1	yes
NGC5548	0.11 ± 0.13	15.95	0.99	1	no
NGC1275**	0.06 ± 0.25	18.22	1	1	yes
2MASXJ11*	1.41 ± 0.19	13.67	0.47	1	no
2MASXJ23*	1.46 ± 0.58	6.35	0.86	1	yes

Table 3.1: Summary of the well-constrained $F_{6.4 \text{ keV}}-F_{2-10 \text{ keV}}$ slopes, the maximum light curve timespan of the observations per source, the P_{var} parameters obtained for the Fe $K\alpha$ line and 2–10 keV continuum light curves of each source and whether the sources are radio-loud AGN. The sources with a star (*) have a slope consistent with one, but do not have highly significant variable light curves for the Fe $K\alpha$ line fluxes. The sources with two stars (**) have a beamed jet (information obtained from Koss et al. (2018)). 2MASXJ11 and 2MASXJ23 correspond to 2MASXJ11315154-1231587 and 2MASXJ23444387-4243124, respectively.

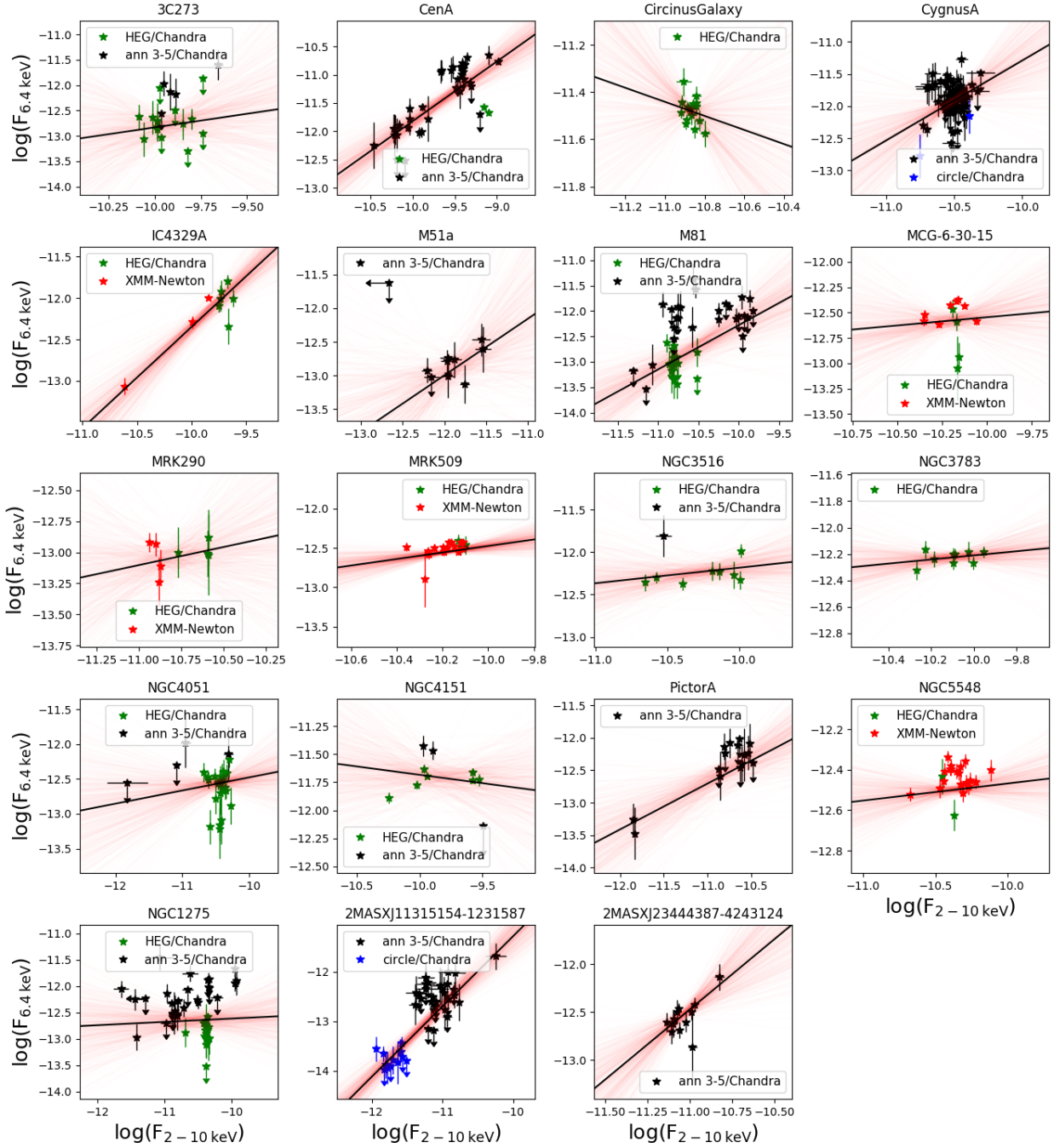


Figure 3.1: Fe $K\alpha$ line flux ($F_{6.4 \text{ keV}}$) against 2–10 keV continuum flux ($F_{2-10 \text{ keV}}$), for the sources with well-constrained $F_{6.4 \text{ keV}}-F_{2-10 \text{ keV}}$ slopes. In the subplots, the green stars are the *Chandra* HEG spectra, the black stars are the *Chandra* ACIS 3''-5'' annular spectra, the blue stars are the 1.5'' circular ACIS spectra and the red stars are the *XMM-Newton* spectra. The values for the slopes are summarized in Figure 3.2. The flux units are $\text{erg cm}^{-2} \text{ s}^{-1}$.

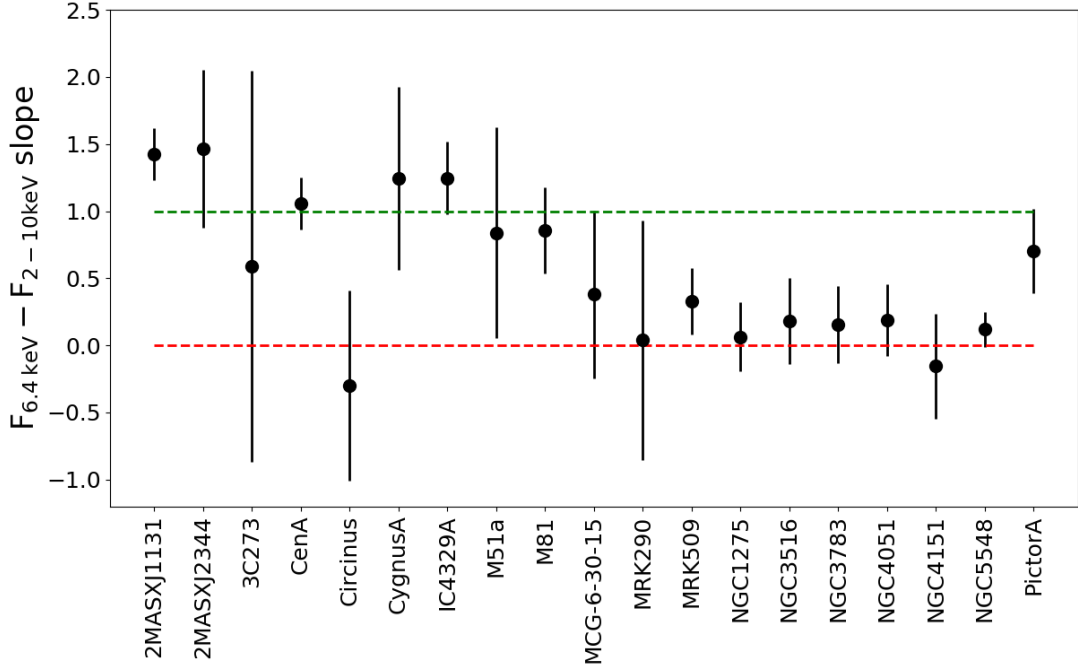


Figure 3.2: $F_{6.4 \text{ keV}} - F_{2-10 \text{ keV}}$ slopes (m) for 19 sources with well-constrained values

We computed the P_{var} parameter, indicating that both light curves are variable. The second plot of Figure 3.1 shows the comparison between these two quantities, which are tightly correlated with a $F_{6.4 \text{ keV}} - F_{2-10 \text{ keV}}$ slope of 1.05 ± 0.19 . The interpretation is similar to the first case mentioned above. For this source, most of the Fe $K\alpha$ line probably originates inside a region with an extension comparable with the light crossing size between the X-ray corona and the reflecting clouds, which for this source is 18 years.

An opposite example is the case of the galaxy NGC 3516. Figure 3.4 shows the light curves for the continuum and Fe $K\alpha$ line fluxes constructed with *Chandra* observations in normal and grating mode, spanning 18 years. We found a maximum variation of around 0.7 dex for continuum flux and around 0.6 dex for the Fe $K\alpha$ line flux. We computed the P_{var} parameter for both light curves and we get that the continuum is intrinsically variable, but the Fe $K\alpha$ line is not. The right middle panel of Figure 3.1 shows the comparison between these two quantities, which in this case are uncorrelated with a $F_{6.4 \text{ keV}} - F_{2-10 \text{ keV}}$ slope of 0.18 ± 0.38 . The interpretation is similar to the second case mentioned above, where probably the reflecting clouds are very distant from the X-ray corona, but alternative explanations are also possible and will be discussed in Section 5.

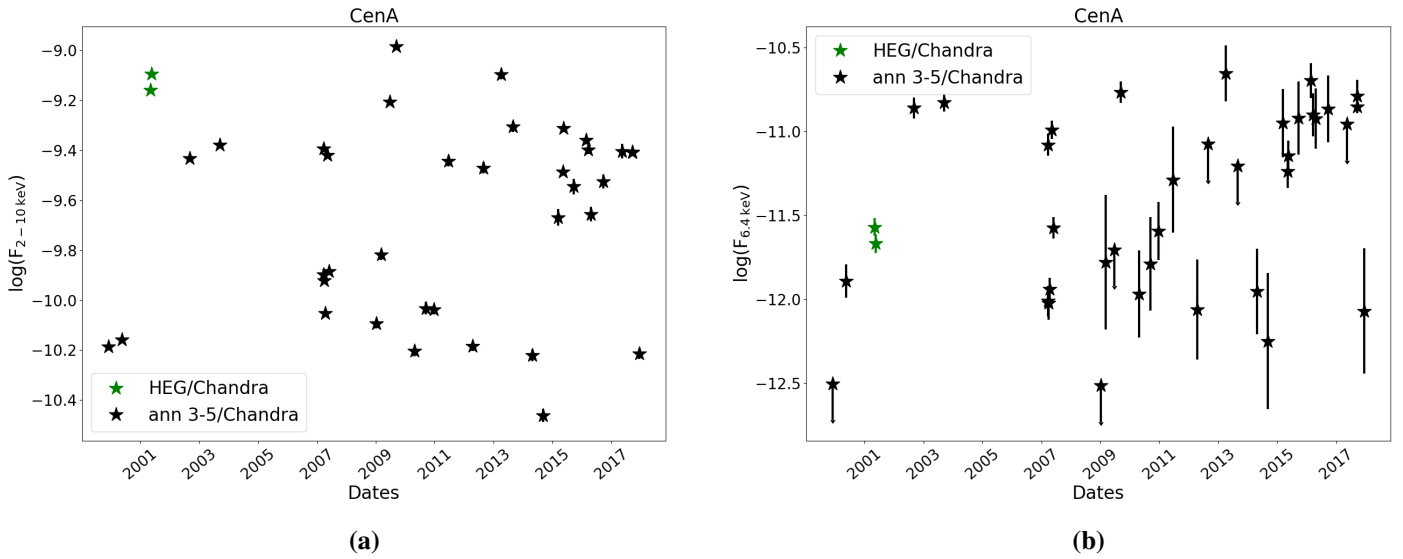


Figure 3.3: Light curves for the 2–10 keV continuum (a) and Fe K α line (b) fluxes for the galaxy Centaurus A. The green and black stars denote fluxes measured from the *Chandra* HEG 1st order spectra and *Chandra* ACIS 3''–5'' annular spectra, respectively.

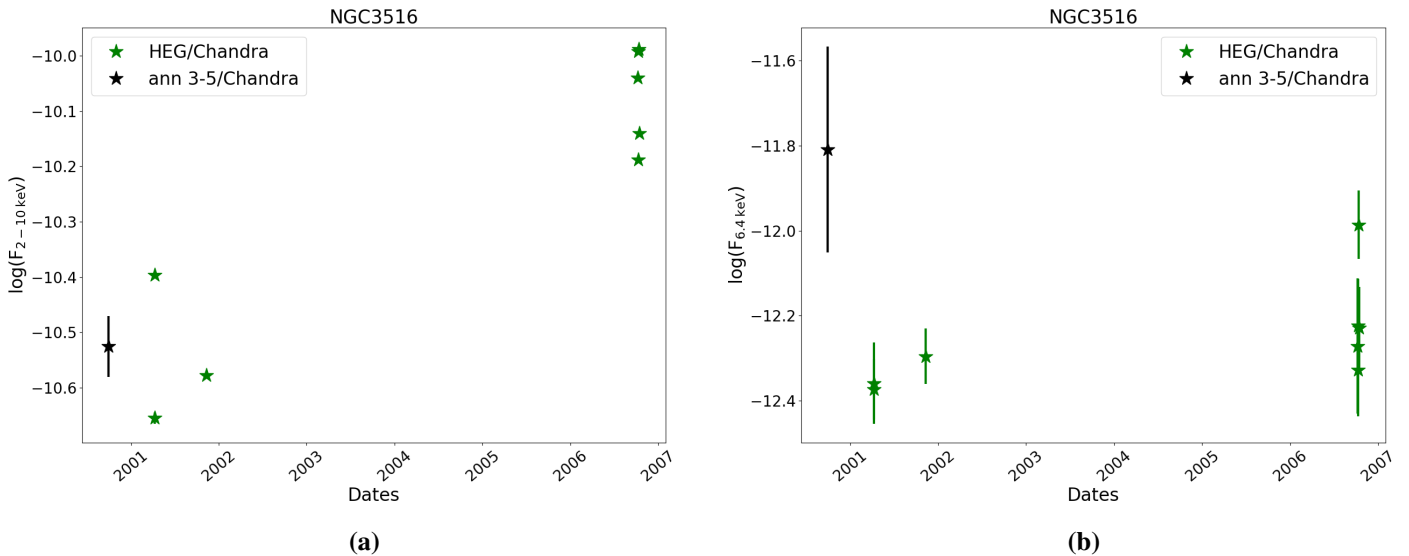


Figure 3.4: Light curves for the 2–10 keV continuum flux (a) and Fe K α line fluxes (b) for the galaxy NGC 3516. The green and black stars are fluxes measured from the *Chandra* HEG spectra and *Chandra* ACIS 3''–5'' annular spectra, respectively.

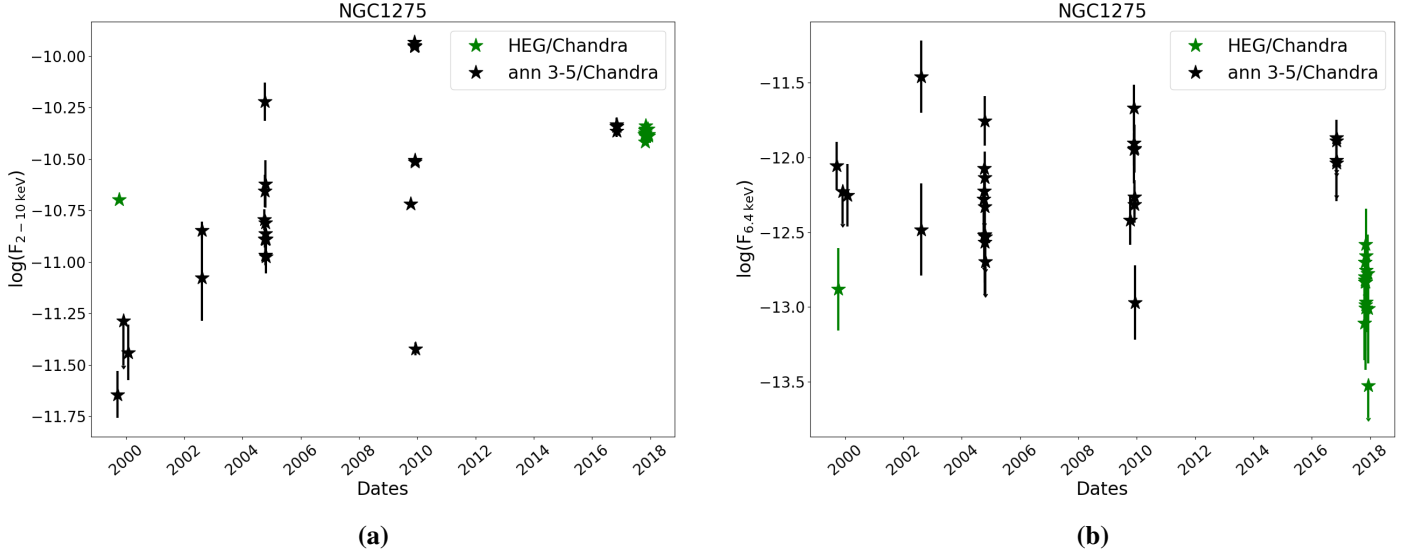


Figure 3.5: Light curves for the 2–10 keV continuum flux (a) and Fe K α line fluxes (b) for the galaxy NGC 1275. The green and black stars are fluxes measured from the *Chandra* HEG spectra and *Chandra* ACIS 3''–5'' annular spectra, respectively.

Another interesting example is the case of the galaxy NGC 1275. Figure 3.5 shows the light curves for the continuum and Fe K α line fluxes, constructed with *Chandra* observations in normal and grating mode, performed over a timespan of 18 years. We found a variation of around two orders of magnitude for both the flux of the continuum and the Fe K α line and the P_{var} parameter suggests that both are intrinsically variable. The bottom left panel of Figure 3.1 shows the comparison between these two quantities, which are uncorrelated with a $F_{6.4 \text{ keV}}-F_{2-10 \text{ keV}}$ slope of 0.063 ± 0.25 . The interpretation is similar to the third case mentioned above, and is discussed in more detail in Section 5.

Figure A.1 and Figure A.2 of the Appendix show light curves for the continuum and Fe K α line fluxes for the rest of the sources with well-constrained $F_{6.4 \text{ keV}}-F_{2-10 \text{ keV}}$ slopes, respectively. Figure A.3 of the Appendix shows the comparison between the Fe K α line and continuum fluxes for sources with unconstrained slopes.

This result indicates that there is not a systematic correlation between the Fe K α line and continuum flux for all AGN, which implies distinct morphological and structural distributions of reflecting clouds among local AGN.

3.2 $F_{6.4 \text{ keV}}-F_{2-10 \text{ keV}}$ slopes constrain problem

From the 280 original galaxies, only 38 possess more than 4 observations. From these sources, only 18 have well-constrained slopes. To understand why the slopes are not well-constrained in nearly half the cases, we compare in Figure 3.6 the size of the error bars of the $F_{6.4 \text{ keV}}-F_{2-10 \text{ keV}}$ slopes as a function of the number of observations (a), the maximum light curve timespan (b), and the ratio of undetected Fe $K\alpha$ line measurements to total measurements (c). From panel (a), it is very clear that the errorbar size depends on the number of observations. Below 9 observations the error values range between ~ 0.2 up to very high values as ~ 7000 , but for more than 10 observations, the error bars take a constant value near or smaller than 1.

Panel (b) presents the errorbars size against the maximum light curve timespan, and shows a mild anti-correlation between them. Panel (c) presents a positive trend, but with a large scatter, between the errorbar size and the percentage of non detected Fe $K\alpha$ lines. At ratios less than 0.4 we have different values for the errorbar, but at ratios higher than ~ 0.4 there are only values higher than 100. Therefore, for our sample, all the sources with more than the $\sim 40\%$ undetected Fe $K\alpha$ line have a $F_{6.4 \text{ keV}}-F_{2-10 \text{ keV}}$ slope unconstrained.

Computing the slopes was a difficult task, since our measurement have asymmetric errorbars and upper-limits, and we could not use any linear regression code to estimate the relation between the fluxes. From the three factors affecting the constraining of the $F_{6.4 \text{ keV}}-F_{2-10 \text{ keV}}$ slopes, the number of observations per source is the most determinant. To increase our sample of well-constrained slopes we should aim to have more than 10 observations per source.

3.3 $F_{6.4 \text{ keV}}-F_{2-10 \text{ keV}}$ slopes compared with AGN and host galaxy properties

To understand the different behaviors of the Fe $K\alpha$ line in our sample, we compared the $F_{6.4 \text{ keV}}-F_{2-10 \text{ keV}}$ slopes with some AGN and host galaxy properties. The data to perform this comparison were mostly obtained from the DR2 of BASS, which is still unpublished, but is an extension of the DR1 results of Koss et al. (2018). BASS DR2 provides information on the bolometric luminosity, the SMBH mass, the equatorial column density, the Eddington ratio, and the Seyfert type.

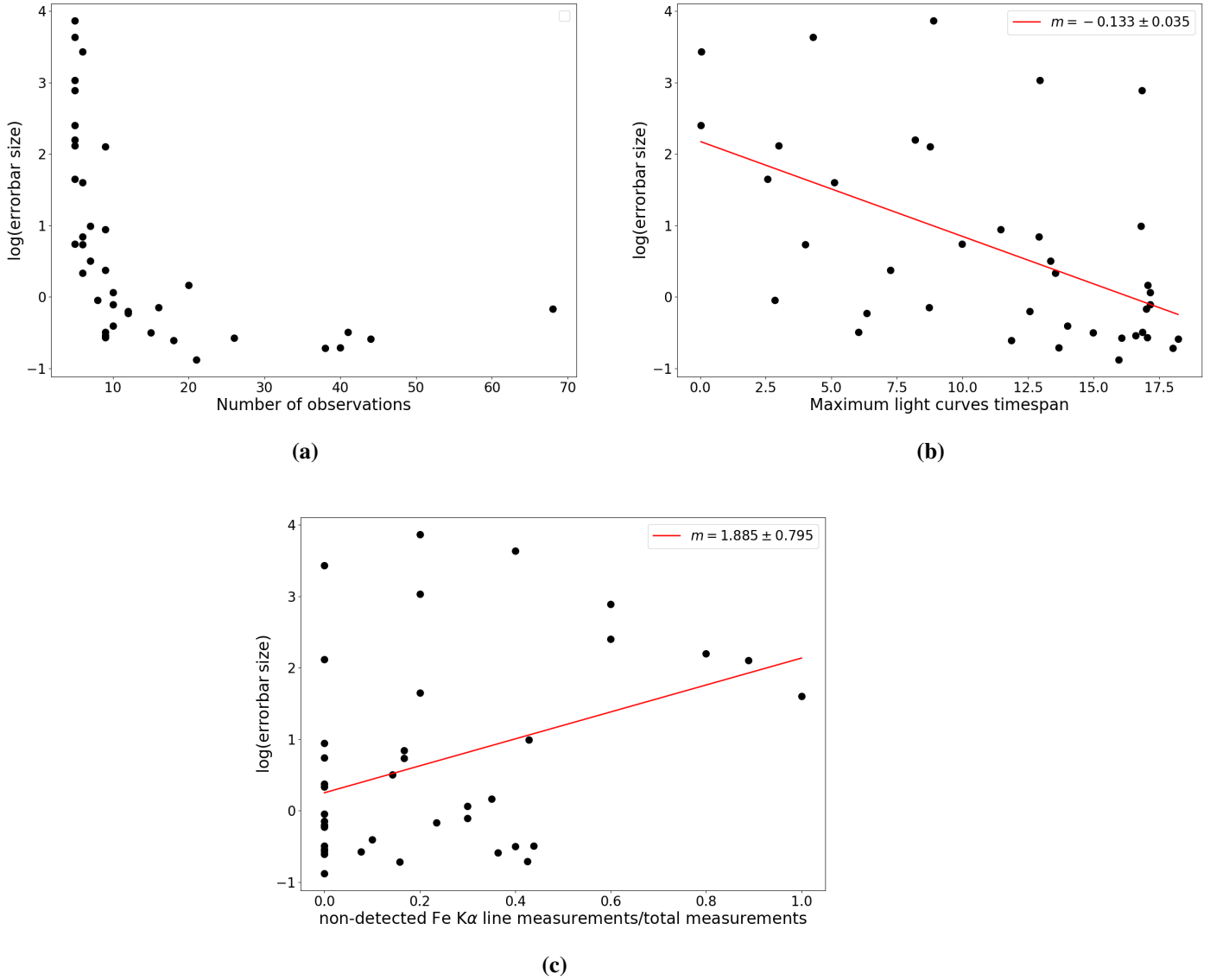


Figure 3.6: Comparison between the size of the $F_{6.4\text{ keV}}-F_{2-10\text{ keV}}$ slopes errorbars and the number of observations (a), the maximum light curve timespan (b) and the non detected Fe $K\alpha$ line flux measurements versus total measurements (c). The orange line is the linear fit of the points and m is the slope of the line obtained for each plot.

A good way to test if we can find any correlation with our data is comparing the $F_{6.4 \text{ keV}}-F_{2-10 \text{ keV}}$ slopes with the ratio between the maximum light curve timespan (T_{lc}) and the dust sublimation radius (R_{sub}). The dusty torus should start beyond R_{sub} , and is where we think most of the X-ray reflection comes from (i.e., from neutral matter, shielded and cooled by dust). Therefore, the aforementioned ratio tells us if our observational timespan is sensitive to correlated changes between the varying X-ray continuum and the Fe $K\alpha$ emission from the inner torus (which would be experience a lag related to the light travel time). The dust sublimation radius is given by

$$R_{sub} = 0.4 \left(\frac{L_{bol}}{10^{45} \text{ erg s}^{-1}} \right)^{1/2} \left(\frac{1500 \text{ K}}{T_{sub}} \right)^{2.6} \text{ pc} \quad (3.1)$$

(Nenkova et al. 2008) where L_{bol} is the bolometric luminosity and T_{sub} is the dust sublimation temperature, generally assumed to be the sublimation temperature of graphite grains, $T \sim 1500 \text{ K}$ (Barvainis 1987).

Figure 3.7 presents the comparison between the slopes and T_{lc}/R_{sub} . All the sources with well-constrained slopes have a value of $\log(T_{lc}/R_{sub}) > 0$, indicating that our observations can probe timescales related to correlated X-ray continuum and torus reflection variations. We found a mild anti-correlation between the $F_{6.4 \text{ keV}}-F_{2-10 \text{ keV}}$ slopes and $\log(T_{lc}/R_{sub})$, but with a large scatter; therefore it is consistent with no correlation. We might expect a correlation between these two quantities if most of the reflection comes from the inner walls of the torus, and if the continuum variability timescales are comparable or larger to the light travel time between the X-ray corona and the inner walls of the torus. Considering that the observations have enough timespan, the non-evident relation between the slopes and $\log(T_{lc}/R_{sub})$ suggests that in some sources the Fe $K\alpha$ line arises from clouds beyond the fiducial torus size scale (perhaps an extended torus or beyond).

Figure 3.8 shows comparisons between the $F_{6.4 \text{ keV}}-F_{2-10 \text{ keV}}$ slopes and different parameters. SubFigure 3.8a presents the relation between the slopes and the central Supermassive black hole mass. Fitting a linear regression between the two quantities, we found a mild relation between them, with slope 0.4 ± 0.182 .

SubFigure 3.8b shows the comparison between the $F_{6.4 \text{ keV}}-F_{2-10 \text{ keV}}$ slopes and the Gini coefficient, which, in an astrophysical context, is a measurement of the non-uniformity of the distribution of light in a galaxy (Florian et al. 2016); we use it here as a proxy to represent the morphology of the AGN host galaxy. We want to test whether large-scale galaxy morphological concentration or

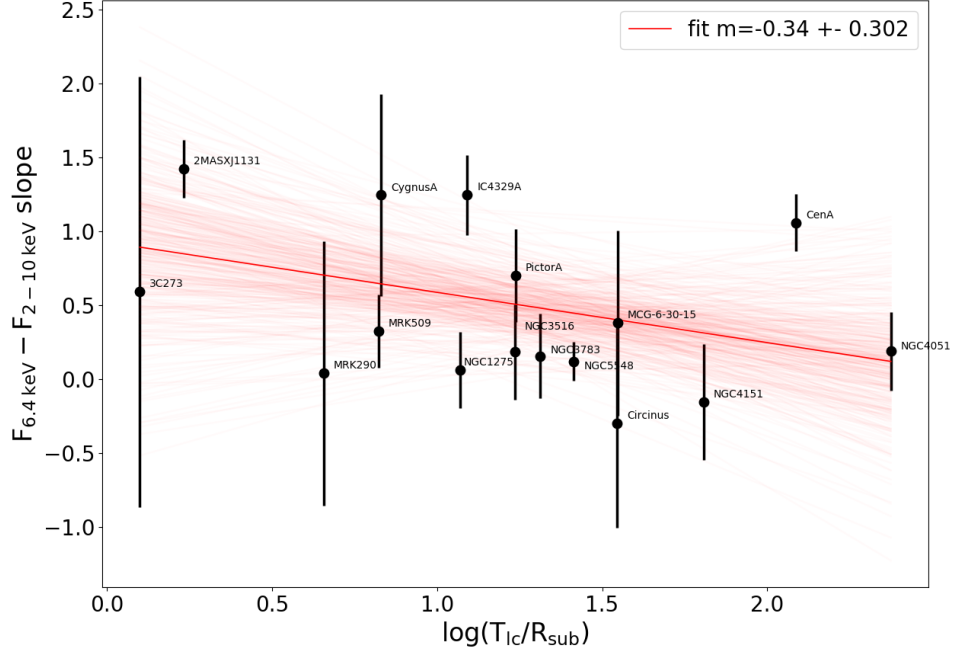


Figure 3.7: Comparison between the $F_{6.4 \text{ keV}} - F_{2-10 \text{ keV}}$ slopes and T_{lc} , which is the ratio between the maximum light curve timespan and the sublimation radius, for all the sources with bolometric luminosity measured.

clumpiness toward the center may correlate with a slopes near to 1. A Gini coefficient close to zero indicates that the distribution of the light is uniform, while a value close to one indicates that most of the light is concentrated in a small area. We computed the coefficient using optical images from the Digitized Sky Survey, for all the sources with well-constrained slopes. We binned all the images to leave them with the same physical resolution ($\sim 1 \text{ kpc/pix}$) using the python package `REBIN` and we computed the Gini coefficient using the python package `STATMORPH`. We made a linear regression between the $F_{6.4 \text{ keV}} - F_{2-10 \text{ keV}}$ slopes and the Gini coefficients and did not find any clear correlation, obtaining a slope $m = 3.922 \pm 5.847$. A positive correlation between these quantities would be expected since the light distribution traces the matter distribution, but the low spatial resolution of the images is not comparable with the AGN scales. It would be interesting to repeat the analysis with higher spatial resolution images.

SubFigures 3.8c, 3.8d and 3.8e present the comparison between the $F_{6.4 \text{ keV}} - F_{2-10 \text{ keV}}$ slopes and the Eddington ratio, the equatorial column density, and the AGN type, respectively. We fitted a linear regression for the first two cases but found no clear trends for any of them.

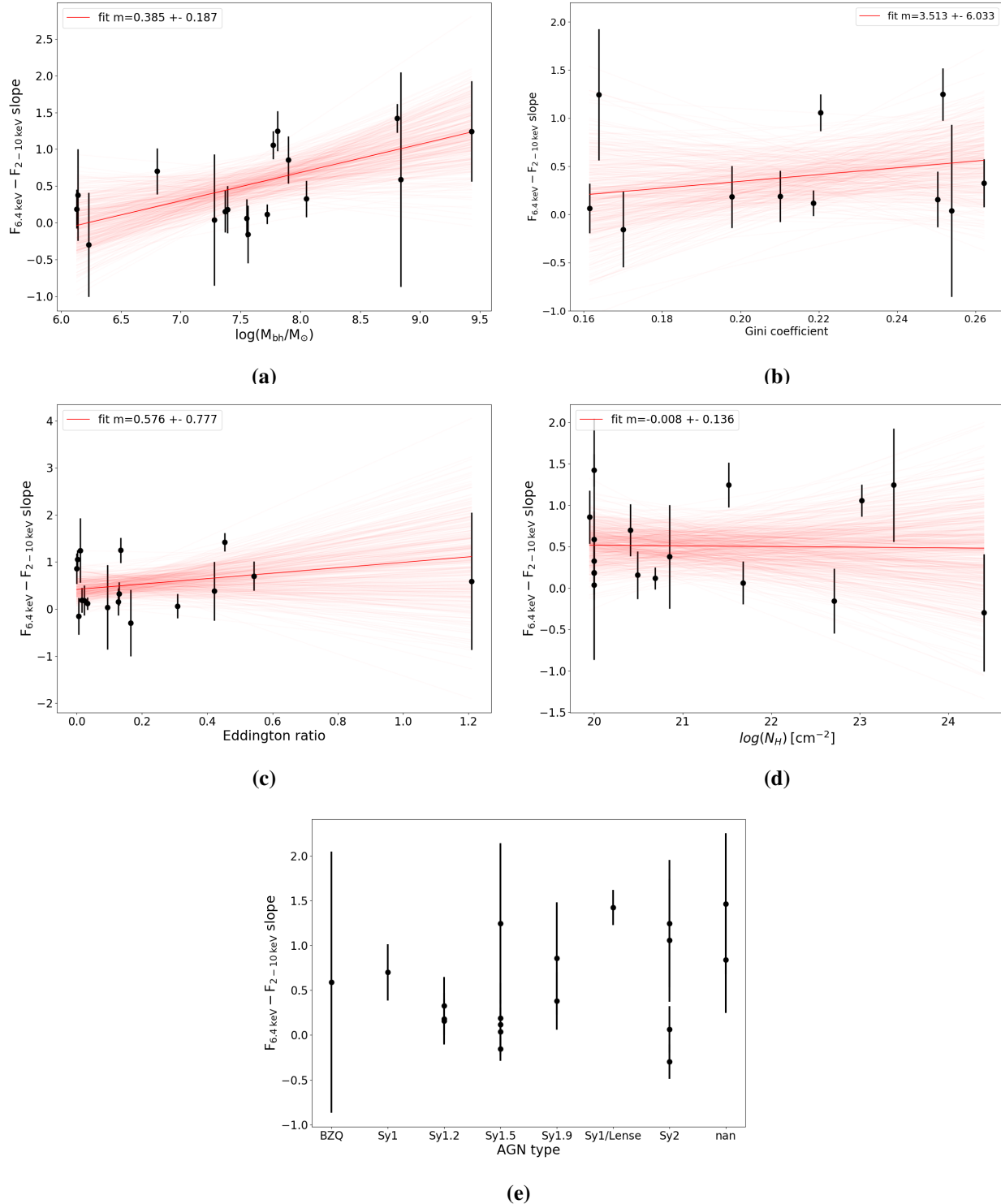


Figure 3.8: Comparison of the $F_{6.4 \text{ keV}} - F_{2-10 \text{ keV}}$ slopes with respect to (a) the Supermassive Black Hole mass, (b) the Gini index, (c) the Eddington ratio, (d) the equatorial column density, and (e) the AGN type. For the first four plots, a linear regression was made between the slopes and the parameter. The slope is indicated in the legend of each plot.

Summarizing, we found a mild correlation between the $F_{6.4 \text{ keV}}-F_{2-10 \text{ keV}}$ slopes and the SMBH mass, and no correlations with the Gini coefficient, Eddington ratio, equatorial column density, or AGN type. Therefore, the only property that might affect the reaction of the Fe $K\alpha$ line to the continuum variations appears to be the SMBH mass.

Chapter 4

Chandra Imaging results

To complement the spectral results above, we carried out an imaging analysis to see whether the sources with well-constrained $F_{6.4\text{ keV}}-F_{2-10\text{ keV}}$ slopes are spatially extended or not, and if the extension is consistent with the slopes obtained in the spectral analysis. In particular, we want to test if the sources with slope near to zero present extended Fe $K\alpha$ emission and if the sources with slope near one are point-like. However, an important issue here is that the *Chandra* PSF wings are not well calibrated. Considering this caveat, we describe our approach to analyze the *Chandra* images below.

4.1 *Chandra* PSF caveats

The point spread function (PSF) describes the shape and size of the image produced by an unresolved source. The *Chandra* PSF is a function of the energy, off-axis angle, and number of source photons, and its shape starts to change dramatically when the off-axis angle is greater than $2'$.

Figure 4.1 shows empirical and simulated PSFs for the X-ray binary Hercules X-1 (HERX1), in two energy ranges. The simulated data were made with the ray-tracing tool MARX (Davis et al. 2012), which simulates the on-orbit performance of the various operations modes of the *Chandra* X-ray Observatory for input source models. It can be seen that for both real and simulated data, the radial profiles show sharp fall-offs in the inner $\sim 10''$ but exhibit broad wings which extend out to large radii. However, from the plot, it is clear that the simulation underpredicts the flux of the

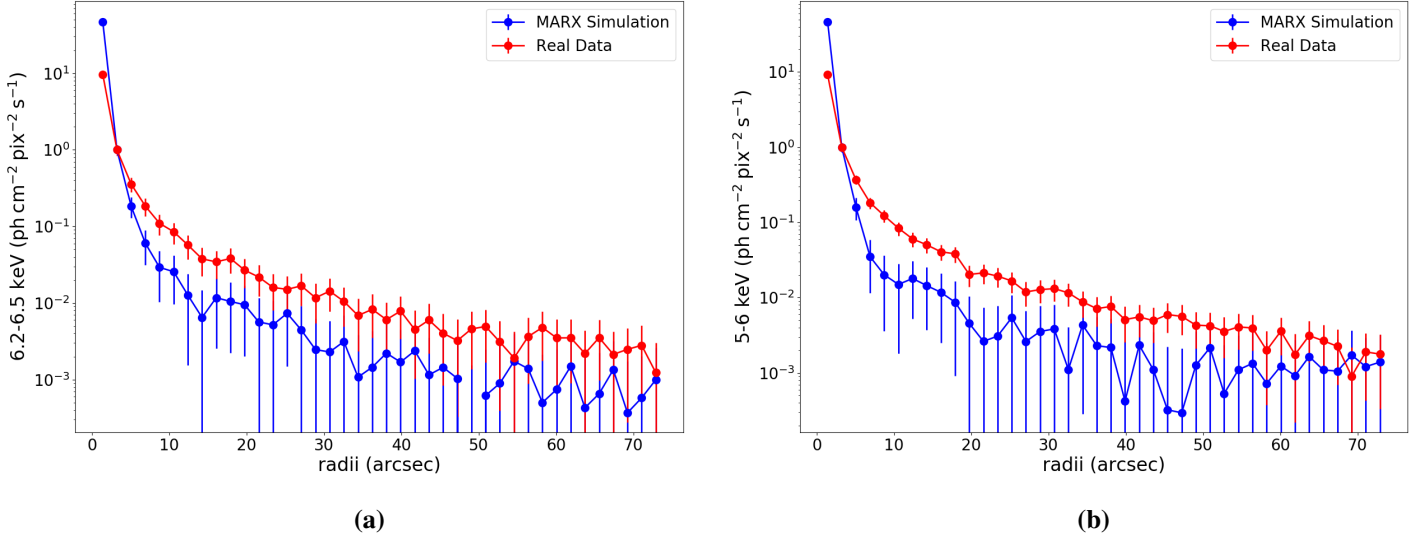


Figure 4.1: Comparison between real and simulated radial profiles for the X-ray binary HERX1. Panels (a) and (b) show radial profiles for the 6.2–6.5 keV and 5–6 keV ranges, respectively. The errors of the real profiles denote 99% confidence, while the errors of the simulated profiles are 97% confidence.

real data beyond $\sim 3''$ – $20''$, depending on the energy range. If improperly modeled (i.e., based on the simulations, which is the only method officially provided by *Chandra*), we could misinterpret point-like emission as extended emission.

Thus to make a proper analysis, we create an empirical PSF from known point-like X-rays sources and compare these radial profiles with those of our AGN sample.

4.2 Empirical PSF and its comparison with our sources

We modeled the PSF using HERX1. We chose this particular source to create an empirical PSF since it is very bright, and therefore has a well-defined profile. The disadvantage of this source is that it is highly affected by pileup in the central $2.5''$; hence we restrict our analysis to outer radii. However, this only has a small impact in our analysis since most of our sources have observations also affected by saturation in the central $\sim 2''$, and we thus are unreliable anyway.

Figure 4.1 presents radial profiles of HERX1 for the 6.2–6.5 keV and 5–6 keV energy bands, in where we can clearly see the wings of the PSF at radii greater than $5''$ – $10''$. Figure 4.2 shows radial profiles for each quadrant of the image, where q1, q2, q3, and q4 are equivalent to quadrant

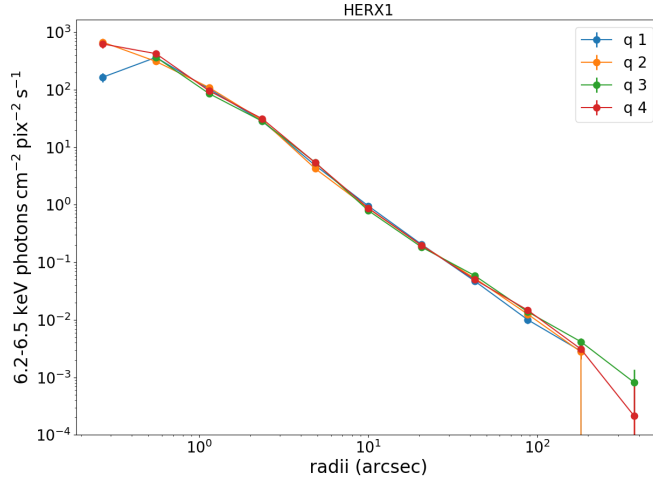


Figure 4.2: Radial profiles for each quadrant of the images of HERX1, in the 6.2–6.5 keV energy range. q1, q2, q3, and q4 are equivalent to quadrant I, quadrant II, quadrant III, and quadrant IV in the coordinate plane. The errors plotted are 97% confidence.

I, quadrant II, quadrant III, and quadrant IV in the coordinate plane; the sense of the quadrants is depicted more clearly in Figure B.3 in the Appendix. It can be observed that the profiles of each quadrant are consistent between them, confirming that the PSF is symmetric. It can be seen a difference between the quadrants in the inner 1'', probably due to a known asymmetry in the PSF at $\sim 0.6''$ – $0.8''$ (caused by an asymmetry HRMA mirrors).

We compared the radial profiles of HERX1 with all the sources with well-constrained $F_{6.4 \text{ keV}} - F_{2-10 \text{ keV}}$ slopes. We excluded the source 2MASXJ11315154-1231587 since it presents 3 lensed images in the field, hindering the contamination subtraction, and we excluded 2MASXJ23444387-4243124 since the source was positioned in a corner of the image, making impossible to generate a profile with radii $> 50''$.

Figure 4.3 shows a comparison between the radial profiles of HERX1 and our sources, for the 6.2–6.5 keV flux range. We did not subtract the continuum here, since the Fe $K\alpha$ emission in some sources is not bright enough to yield good statistics. To make a proper comparison, we normalized each profile with the flux at the lowest radius without pileup. If we normalize in a larger radius, we could be normalizing out some extended emission. We calculated this radius in the same way we classified pileup and non-pileup observations, using equation 2.2 (see Section 2.2.2), but this

time using several annulus from $0''$ - $0.5''$ to $7''$ - $7.5''$. We take in account the possible fake low counts per second in the central arcseconds due to the saturation in very bright sources, to decide the free-pileup radius. The green dotted line on each plot represents the normalization radii, which in most cases is $r = 2.5''$. It can be seen that for most of the sources the profiles are consistent with the profile of HERX1, except for Cygnus A and NGC1275. For the former, the inconsistency is due to jets contamination, the hotspot and diffuse emission from the galaxy cluster which the galaxy is embedded, which is very difficult to remove, while for the latter is affected by the emission of Perseus galaxy cluster which the galaxy is centrally embedded. For these reasons, we will not consider these 2 galaxies for our analysis. The fact that the remaining 15 galaxies have 6.2–6.5 keV radial profile consistent with that of HERX1 suggests that the Fe $K\alpha$ emission comes from a point-like source and is not spatially extended.

Figure 4.4 shows the radial profiles for each quadrant of the images, for all the sources. The plots indicate that in most sources the radial profiles are consistent between the quadrants, suggesting that the sources are symmetric. The exceptions are MCG-6-30-15 and NGC 4051, which have some quadrants with more flux than others around $\sim 2''$. To find out whether this extension is due to non-reported contamination sources or PSF artifact, we made radial profiles for other energy ranges. Figure B.1 of the Appendix depicts radial profiles for each quadrant, but for the flux in the 2.5–3 keV range, showing that all the sources look symmetric in those energies. The symmetry of radial profiles in the 2.5–3 keV range suggests that the extensions observed in the 6.2–6.5 keV profiles are not due to contamination sources in the field, otherwise we would expect the extension around $2''$ in all the energy ranges. The extension should not be a PSF artifact since we observed it only in some sources.

To confirm whether in some quadrants the extension is real, we subtracted the 6.2–6.5 keV continuum and we analyzed only the Fe $K\alpha$ photons. Figure B.2 of the Appendix shows the Fe $K\alpha$ flux radial profiles for each quadrant. For most of the sources, the statistic is very bad and only for NGC 4051 we can confirm that there are quadrants with more flux than others around $2''$ - $3''$.

Figure B.3 of the Appendix shows the image of the Fe $K\alpha$ photons for NGC 4051, with marks for the quadrants and two circles with radii $2''$ and $4''$. From the image is clear that quadrant IV has significantly fewer counts than the other ones and that there is a mild asymmetry around 1 - $4''$.

Using the facts that all of our sources but NGC 4051 are symmetric and their profiles are

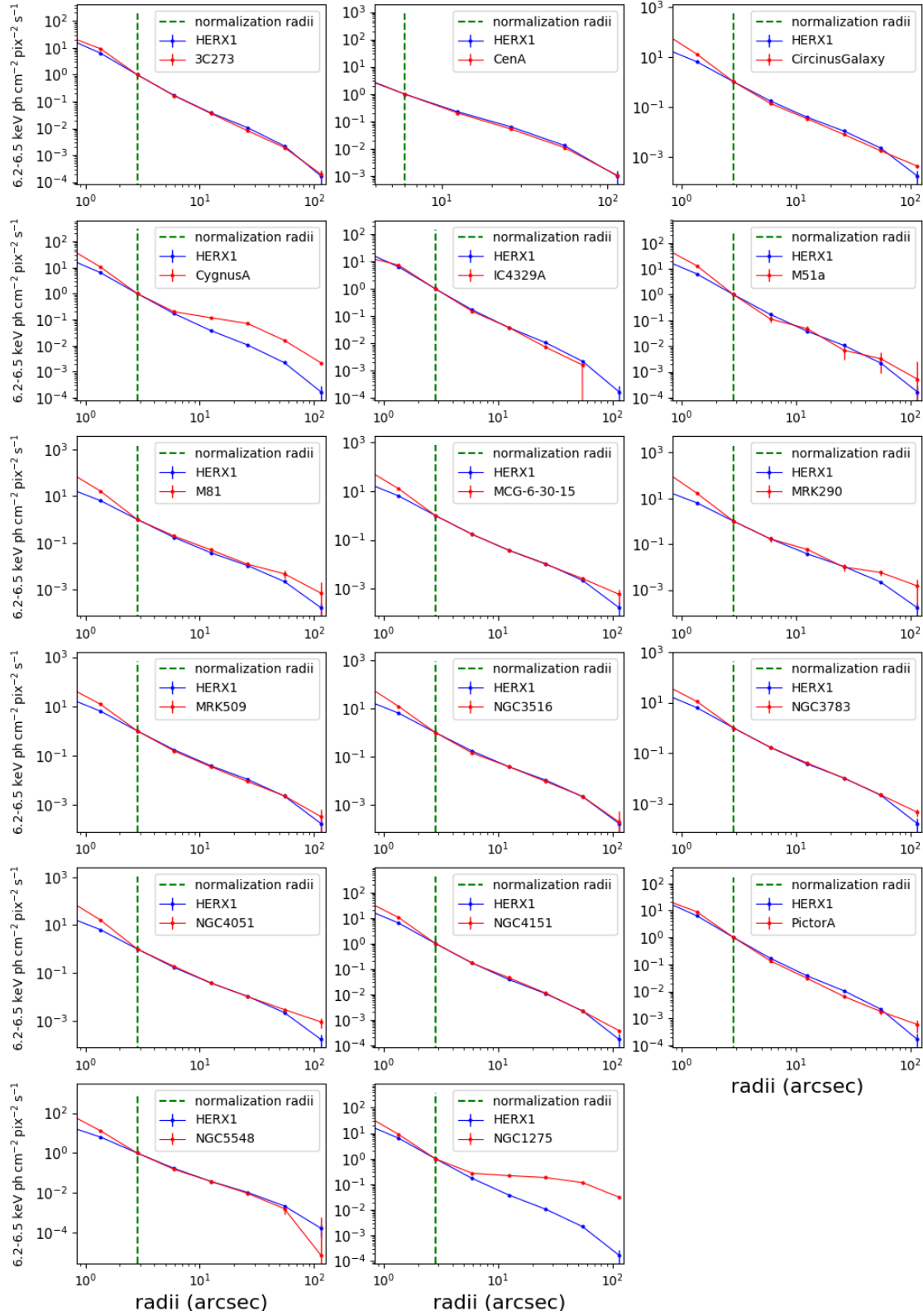


Figure 4.3: Comparison between the 6.2–6.5 keV radial profile of HERX1 (blue points) and our sources with well constrained $F_{6.4 \text{ keV}} - F_{2-10 \text{ keV}}$ slopes (red points). The green dotted line on each plot represents the free pileup radii used to choose the normalization flux for each profile.

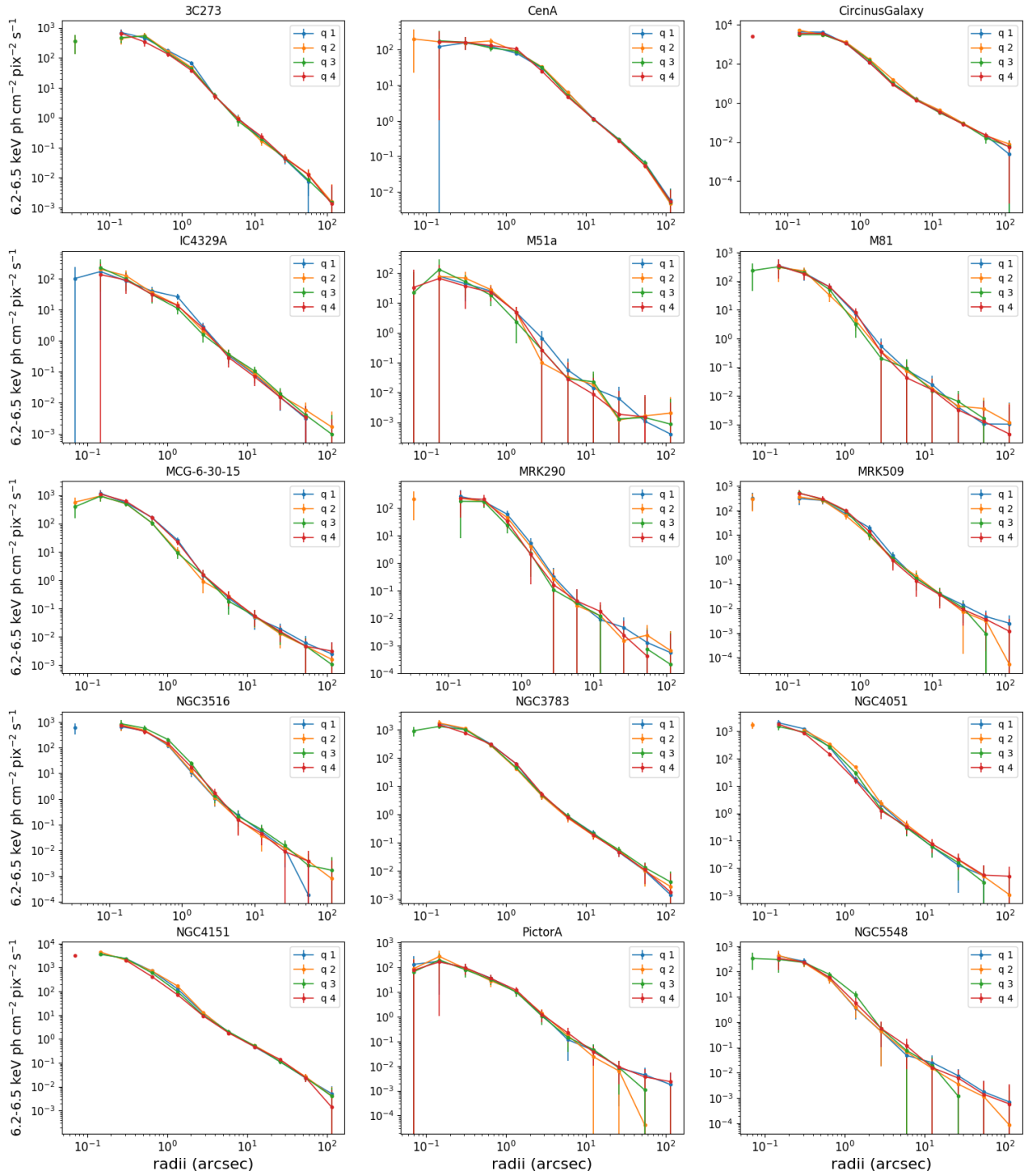


Figure 4.4: Radial profiles for each quadrant of the images, for all the sources with well constrained $F_{6.4 \text{ keV}} - F_{2-10 \text{ keV}}$ slopes (except the ones with difficult contamination subtraction). The profiles are for the flux in the 6.2–6.5 keV range. q1, q2, q3, and q4 are equivalent to quadrant I, quadrant II, quadrant III, and quadrant IV. The errors plotted are 99% confidence.

consistent with HERX1, we can assure that their Fe $K\alpha$ emission is point-like .

4.3 The case of NGC 1068

Despite we could not constrain the $F_{6.4 \text{ keV}}-F_{2-10 \text{ keV}}$ slope of NGC 1068, this source is a useful object to study since it has a clear extension along the ionization cone. The spatial extension of this source was discussed by (Bauer et al. 2015), but no analysis with respect to the extension was made.

Figure 4.5a depicts the comparison between the radial profile of HERX1 and NGC 1068 for the 6.2–6.5 keV range. A difference can be seen between the profiles around $10''$, but it is not striking, and for the rest of the radii the profiles seem consistent. Figure 4.5b shows the radial profiles for the Fe $K\alpha$ photons for each quadrant of the NGC 1068 image. Quadrant IV has more flux than the other ones between $\sim 2.5''-15''$, and quadrant II has a flux consistent with quadrant IV around $10''$.

Figure B.4 of the Appendix presents radial profiles per quadrants from 2.5 keV until 6 keV with a 0.5 keV step. For all the energy bins asymmetry is observed, and quadrant II and IV always have more flux than quadrant I and III. On the other hand, it can be seen how the profiles change with the energy: the profiles of the central arcsecond seem consistent for energies lower than 5 keV, but start to show a difference for energies higher than 5 keV. The asymmetry observed in the profiles supports the fact that NGC 1068 is really extended. We did not observe this behavior in any of the sources of our sample, which confirms that none of our sources with well-constrained $F_{6.4 \text{ keV}}-F_{2-10 \text{ keV}}$ slopes are spatially extended for all energies. Figure 4.6 shows an image for the 2–10 keV emission of NGC 1068, from where we can clearly see the extension along quadrants II and IV.

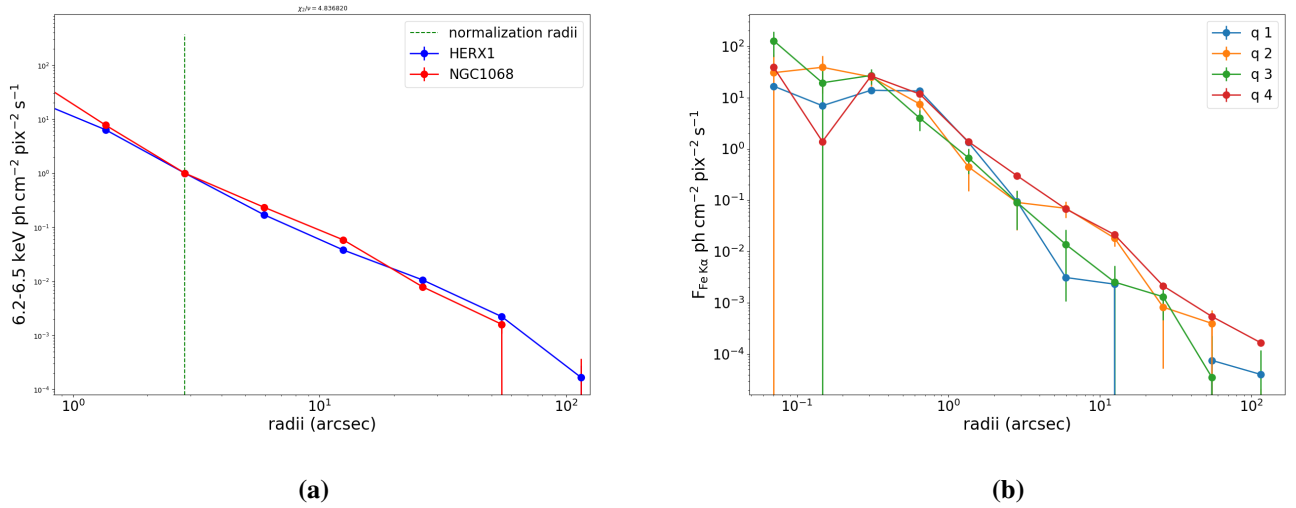


Figure 4.5: Radial profiles of the 6.2–6.5 keV flux of NGC 1068. The panel (a) shows the comparison between the profile of HERX1 and NGC 1068. The profiles are normalized with the flux at the free pileup radii marked by the green line. The panel (b) shows the 6.2–6.5 keV radial profiles for each quadrant of the images at 97.7% confidence error.

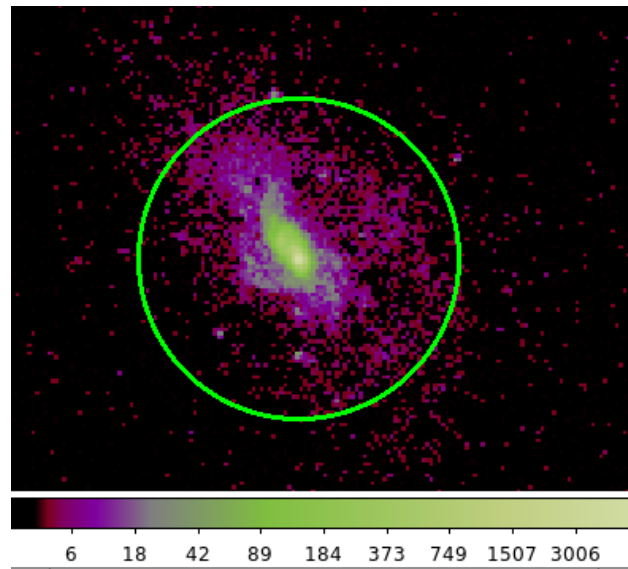


Figure 4.6: *Chandra* image for the 2–10 keV emission of NGC 1068. The green circle marks the inner 20'' region.

Chapter 5

Discussion

We carried out spectral and imaging analysis of 19 AGNs with well constrained $F_{6.4 \text{ keV}}-F_{2-10 \text{ keV}}$ slopes using *Chandra* and *XMM-Newton* observations.

In Chapter 3 we showed that the Fe $K\alpha$ line flux has different behaviors in our sample, which can be summarized in three cases. First, for some sources the line reacts quickly to continuum variations, suggesting that the Fe $K\alpha$ emission originates relatively close to the X-ray emission source (e.g., clouds associated with disk winds, BLR, or inner walls of the torus). Second, in other cases the Fe $K\alpha$ line flux does not react to continuum variations in the observations timescales, indicating that the Fe $K\alpha$ emission arises from an extended region at larger scales (e.g., several R_{sub} from the SMBH). Third, some AGN show variability in both the Fe $K\alpha$ line emission and the continuum, but the fluxes are not correlated, suggesting a more complex picture. In these cases, we cannot provide a limit for the location of reflecting material. Figure 3.7 demonstrates that we can measure the interaction between the X-ray continuum and the dusty torus for our sample, indicating that our data is sensitive to find correlations.

We can constrain the location of reflecting clouds for the sources with a $F_{6.4 \text{ keV}}-F_{2-10 \text{ keV}}$ slopes fully consistent with one (e.g, 2MASXJ11315154-1231587, 2MASXJ23444387-4243124, Centaurus A, IC4329A and M81). These AGN have different values for the $\log(T_{\text{lc}}/R_{\text{sub}})$, going from ~ 0.2 to ~ 2.1 , indicating that the reflecting clouds are inside of a region of size of 1.5 to ~ 125 times the sublimation radius (or 4.19 to 5.22 pc). These regions may be any component of the AGN inside that radius, as someplace in the torus and/or clouds associated with the BLR and accretion disk. For sources with $F_{6.4 \text{ keV}}-F_{2-10 \text{ keV}}$ slopes consistent with one but only as an upper

limit or due to large errorbars (e.g, Cygnus A, M51a, M81, PictorA), an important fraction of Fe $K\alpha$ emission may arise from a region inner to the light crossing sizes measured in the observations timescales, but there is another fraction that may come from larger scales, thereby weakening the variability signal. Therefore, for these sources, the location of reflecting clouds is inconclusive.

From the *Chandra* imaging analysis we could analyze 15/19 sources with well-constrained $F_{6.4\text{ keV}}-F_{2-10\text{ keV}}$ slopes. We concluded that all these sources but NGC 4051 are point-like, thus they do not have Fe $K\alpha$ extended emission, hence we can use the spatial resolution of *Chandra* (0.5 arcseconds) to provide an upper limit for the reflecting region. For the closer sources (eg., M81, Circinus Galaxy, M51a) the upper limit obtained is lower than 20 pc, while for the farther (eg., MRK 290, MRK 509, 3C273) the upper limit for the torus regions is greater than 300 pc. Table 5 summarizes the upper limits computed for our sample using the spectral and imaging analysis.

We obtained $F_{6.4\text{ keV}}-F_{2-10\text{ keV}}$ slopes ~ 0 and non-variability in the Fe $K\alpha$ line fluxes for MRK 509, NGC 3516, and NGC 3783. For these sources, the interpretation is that the reflecting clouds locate in an extended zone, much farther from the X-ray corona, and we could provide a lower limit for them (i.e., the light crossing size during the observations timescales) if these were the situation, but alternative explanations are also possible. Another hypothesis to explain the lack of Fe $K\alpha$ variability in timescales of years could be the ionization of parsec-scales material; which will suppress the Fe $K\alpha$ emission in that region, continuum variability timescales much more shorter than the light travel time between the corona and the reflecting material, a very low covering factor of the reflecting clouds causing a mild reaction of the Fe $K\alpha$ line to continuum variations and/or clumpiness in the reflecting material diminishing the reaction of the Fe $K\alpha$ flux. To test some of these hypothesis we need to study the line shape to know whether is consistent with originates at larger scales or near to the SMBH, and the continuum variability timescales.

The lack of correlation between the Fe $K\alpha$ line and continuum fluxes when both vary suggests a complex picture for the X-ray reflection and may be related with some of the hypothesis mentioned above, as with the reflector geometry and/or spectral complexity. Several studies have contributed to explain the lack of correlation between these quantities. Ross et al. (1999) and Nayakshin & Kallman (2001) showed that when the X-ray continuum is in a high state, outer layers of the accretion disk are ionized, leading to suppression of the broad and medium velocity components of the Fe $K\alpha$ emission. Iwasawa et al. (1996) suggest that the complex variability of the Fe $K\alpha$

Source	Upper limit (pc) - spectral analysis	Upper limit (pc) - imaging analysis
2MASXJ11	4.19	–
2MASXJ23	1.95	–
3C273	–	1419.28
Centaurus A	5.53	19.66
Circinus Galaxy	–	15.61
CygnusA	5.21	–
IC4329A	5.22	169.94
M51a	–	16.63
M81	5.2	1.21
MCG-6-3-15	–	82.87
MRK290	–	307.98
MRK509	–	356.08
NGC3516	–	94.36
NGC3783	–	103.79
NGC4051	–	–
NGC4151	–	35.69
NGC5548	–	181.56
NGC1275	–	–
PictorA	–	362.63

Table 5.1: Upper limits for the reflecting clouds emitting Fe $K\alpha$ photons found with the spectral and imaging analysis.

line is due to multiple X-ray sources flaring at different radii above the disk. In the same line, Nayakshin & Kazanas (2002) found that when the X-ray flaring events are far from the accretion disk surface and the disk is ionized, the relaxation time to return to a hydrostatic balance in the disk is larger than continuum variation timescales, and therefore the Fe $K\alpha$ line and continuum fluxes are uncorrelated. Vaughan & Edelson (2001) used this fact to argue that multiple flaring regions illuminating a relatively small area of the disk may produce this lack of correlation between the fluxes, and when the AGN enters a prolonged low state, the Fe $K\alpha$ flux should respond. Ballantyne & Fabian (2001) showed that the variation of the Fe $K\alpha$ line flux can be explained by a model with more than one X-ray emission region.

Another possibility which could explain the lack of correlation between the fluxes is the presence of unresolved X-ray binaries (XRBs) or ultraluminous X-ray sources (ULXs) in the field, overlapping their emission with the AGN. For the imaging analysis, we needed to remove several point-like X-ray sources very close to the nucleus (see Figures 2.2 and 2.6), some of them have been previously reported as XRBs/ULXs (e.g., Circinus Galaxy (Bauer et al. 2001; Walton et al. 2013)). The presence of XRBs near to the AGN is expected since the XRB number scales with the star formation rate and host galaxy stellar mass (e.g., Zhang et al. 2012; Lehmer et al. 2019). In the case of ULXs, they can contribute to the continuum variability, but may only generate weak reflection if they are strongly beamed (as is thought to be the case for ULXs with confirmed neutron star periods (e.g., King & Lasota 2016)). Unresolved ULXs or XRBs could explain the lack of correlation between the Fe $K\alpha$ line and continuum fluxes if their luminosities were comparable with the AGN luminosities, which for our sample are $L_x > 10^{42} \text{ erg s}^{-1}$ (Koss et al. 2018). Based on the expected XRB luminosity function for AGN hosts, the vast majority of XRB have $L_x \lesssim 10^{39} \text{ erg s}^{-1}$, with only a very small fraction (<1 on average per galaxy) with luminosities extending up to $10^{41} \text{ erg s}^{-1}$ (e.g., Zhang et al. 2012; Lehmer et al. 2019). Thus, the luminosity limits of our AGN allow us to rule out dominant contributions to the X-ray variability from ULXs/XRBs.

The contribution of the jet in radio-loud AGN can also affect the correlation between the continuum and Fe $K\alpha$ fluxes. 3C 273 has large errorbars on the $F_{6.4 \text{ keV}}-F_{2-10 \text{ keV}}$ slope despite having 20 observations. The difficulty of constraining the slope could be explained by its beamed jet, which might contribute to the continuum variability in higher proportions than to the line variability, similar to the ULX case. NGC 1275 also has a beamed jet, which could explain the lack

of correlation between the continuum and Fe $K\alpha$ fluxes.

Another factor that could affect the lack of correlation between the fluxes is the simplicity of our spectral model, which fit the X-ray emission with a powerlaw, a Gaussian and photoelectric absorption, this could hide correlated variability of the continuum and/or Fe $K\alpha$ emission. More complex models can incorporate the modeling of neutral and/or ionized reflection, ionization state and specific geometries of the absorbing/reflecting material, etc, reproducing more precisely the fluxes (e.g., Zoghbi et al. 2019). On the other hand, using our simple model, we find strong correlation in many AGN, whereby the flux of the line proportionally reacts to continuum variations.

As a point of comparison, several previous studies found a lack of correlation between the Fe $K\alpha$ line and continuum fluxes for a few of the sources in our sample, but on different timescales. Vaughan & Edelson (2001) analyzed the X-ray spectra of MCG-6-30-15 using a 4-day ASCA observation, and found a lack of correlation between the fluxes, yet significant variability in both, and a broad line shape suggesting that the bulk of the Fe $K\alpha$ emission arises close to the SMBH. Chiang et al. (2000) studied the NGC 5548 spectra using 4 different observations performed within 30 days by EUVE, ASCA, and RXTE, and found a constant line flux while the continuum is variable, but a line shape consistent with a substantial fraction of the iron emission originating from within $\sim 20r_g$ from the corona. Tombesi et al. (2007) analyzed multiple *XMM-Newton* observations for NGC 3783 and found that the Fe $K\alpha$ core remained constant during continuum variations but presented a redshifted wing which was correlated with the continuum, suggesting that a portion of the line arises from a relativistic region near the SMBH. These studies are generally consistent with our findings.

Different studies have obtained different conclusions with respect to the location of the Fe $K\alpha$ emitting regions. Gandhi et al. (2015) analyzed 13 local Type 1 AGN and argued that the dust sublimation radius is an outer envelope for the narrow Fe $K\alpha$ emission, suggesting that the bulk of the Fe $K\alpha$ line has an upper limit in the inner wall of the torus and may originate in clouds associated with the BLR or even further inside. Contrarily, Nandra (2006) showed that no correlation exists between the Fe $K\alpha$ core width and the BLR line width, concluding that typically the Fe $K\alpha$ core originates in regions outside the BLR, probably in the inner edge of the torus. Shu et al. (2011) presented an extensive analysis of Fe $K\alpha$ cores in 36 sources and found that there is not a universal location for the Fe $K\alpha$ line emitting regions, since a particular source may have contributions to

the Fe $K\alpha$ line flux from parsec-scale distances from the SMBH, down to regions inside the BLR. Marinucci et al. (2012) presented a time, spectral, and imaging analysis of NGC4945 and showed that the reflecting structure is at a distance $\geq 30 - 50$ pc, much larger than the typical torus scales. Then, in a later investigation, (Marinucci et al. 2017) concluded that the Fe $K\alpha$ emission is extended up to hundreds of parsecs.

This work supports the hypothesis that there is not a particular location for the reflecting clouds emitting Fe $K\alpha$ photons and it reconciles all the previous investigations about the location of the Fe $K\alpha$ emitting regions. For some AGN, the emission arises from clouds associated with the BLR or the inner walls of the torus, for others, the clouds are factor of hundreds beyond the sublimation radius.

Chapter 6

Conclusions and future work

In this work we analyzed observations for 38 AGN from *Chandra* and *XMM-Newton* observatories to constrain the neutral reflecting material in AGN, by studying the Fe $K\alpha$ line emission behavior through a spectral and imaging analysis. We created light curves for the Fe $K\alpha$ line and the continuum between 2–10 keV and then fitted linear regressions to estimate the $F_{6.4 \text{ keV}} - F_{2-10 \text{ keV}}$ slopes for all our sources. We were able to constrain the slopes for 19 AGN, which all show continuum variability, but only five of them show clear Fe $K\alpha$ variability. We obtained three different behaviors:

1. 5 sources exhibited $F_{6.4 \text{ keV}} - F_{2-10 \text{ keV}}$ slopes consistent with one. These AGN have reflecting clouds located near to the X-ray corona, in a compact zone, and the Fe $K\alpha$ line reacts to continuum variation in the light curves timespan. Additionally, there are others 5 sources with slopes consistent with one but large errorbars, suggesting that a portion of the line arises near to the nucleus, and another portion originates at larges scales.
2. 3 sources had $F_{6.4 \text{ keV}} - F_{2-10 \text{ keV}}$ slopes consistent with zero, variable light curves for continuum flux, and constant light curves for the Fe $K\alpha$ emission. The most probable explanation is that these AGN have reflecting clouds far enough the X-ray corona so that the Fe $K\alpha$ line flux does not react to continuum variation in the maximum light curve timespan. Alternative interpretations remain a very low covering factor and/or a clumpy structure which could diminish the Fe $K\alpha$ reaction, and timescales of the continuum variability much more rapid than the light travel time to the reflector.

3. 6 sources had $F_{6.4 \text{ keV}} - F_{2-10 \text{ keV}}$ slopes consistent with zero and variable light curves for both the continuum and Fe $K\alpha$ fluxes. The picture for these sources is more complex and possible explanations may be ionized accretion disk, or multiple hot spot in an extended corona.

Additionally, a possibility to explain the lack of correlation between the fluxes for 3C 273 and NGC 1275, might be the presence of the beamed jet, which affects the continuum variability in higher proportions than the line variability.

We looked for correlations between the $F_{6.4 \text{ keV}} - F_{2-10 \text{ keV}}$ slopes and some AGN and host galaxy properties, specifically SMBH mass, Gini coefficient, Eddington ratio, equatorial column density and AGN type. We only found a mild correlation with the SMBH mass, suggesting that at larger masses the reflecting clouds are located closer to the X-ray corona.

We detected an inconsistency between the real and simulated *Chandra* PSF beyond $\sim 3'' - 20''$, where the simulations underpredict the real data. This explains the calibration constant found between the HEG and $3'' - 5''$ annular spectra of 0.424 ± 0.00507 , instead of one, as it should be if the PSF correction was accurate. To analyze the images of our sources, we created empirical PSF using the X-ray binary HERX1. From the 19 sources with well-constrained slopes, we were able to analyze the *Chandra* images for 15 AGN. We concluded that the radial profiles of the Fe $K\alpha$ emission are consistent with point-like sources for all the sources but NGC 4051. Using this fact, we provided an upper limit for the reflecting clouds equivalent to $0.5''$ (~ 1.21 to 1419 pc).

From the 38 galaxies (with more than 5 points) of our sample, we were able to constrain the Fe $K\alpha$ - continuum relation for 19 of them. Presently, there are more *XMM-Newton* spectra available that we did not add in this project, which could increase the well-constrained galaxies. We aim to consider the new data in the publication of this work.

Our results indicate that we still need to understand many things to explain the neutral reflection in AGN, and there is much more analysis we could make in the future with our data. For example, it would be interesting to study in more detail the variability timescales of our light curves, to test if the line flux is constant due to the very rapid variation of the continuum, and to obtain information about the location of the reflecting clouds through the variability timescales of the Fe $K\alpha$ line. Also, for the sources with $F_{6.4 \text{ keV}} - F_{2-10 \text{ keV}}$ near to one we could measure the time delay between the Fe $K\alpha$ line and the continuum to estimate with more precision the location and extension of the emitting regions.

Bibliography

Arévalo P., et al., 2014, ApJ, 791, 81

Arnaud K. A., 1996, in Jacoby G. H., Barnes J., eds, Astronomical Society of the Pacific Conference Series Vol. 101, Astronomical Data Analysis Software and Systems V. p. 17

Asmus D., Hönic S. F., Gandhi P., Smette A., Duschl W. J., 2014, MNRAS, 439, 1648

Ballantyne D. R., Fabian A. C., 2001, MNRAS, 328, L11

Barvainis R., 1987, ApJ, 320, 537

Bauer F. E., Brandt W. N., Sambruna R. M., Chartas G., Garmire G. P., Kaspi S., Netzer H., 2001, AJ, 122, 182

Bauer F. E., et al., 2015, ApJ, 812, 116

Beckmann V., Shrader C., 2012, in Proceedings of “An INTEGRAL view of the high-energy sky (the first 10 years)” - 9th INTEGRAL Workshop and celebration of the 10th anniversary of the launch (INTEGRAL 2012). 15-19 October 2012. Bibliotheque Nationale de France, Paris, France. Published online at <http://pos.sissa.it/cgi-bin/reader/conf.cgi?confid=176>, id.69. p. 69 (arXiv:1302.1397)

Bianchi S., Guainazzi M., Matt G., Fonseca Bonilla N., 2007, A&A, 467, L19

Blandford R. D., 2001, Progress of Theoretical Physics Supplement, 143, 182

Bondi H., 1952, MNRAS, 112, 195

- Brandt W. N., Alexander D. M., 2015, *A&ARv*, 23, 1
- Cackett E. M., Zoghbi A., Reynolds C., Fabian A. C., Kara E., Uttley P., Wilkins D. R., 2014, *MNRAS*, 438, 2980
- Canizares C. R., et al., 2000, *ApJ*, 539, L41
- Chiang J., Reynolds C. S., Blaes O. M., Nowak M. A., Murray N., Madejski G., Marshall H. L., Magdziarz P., 2000, *ApJ*, 528, 292
- Davis J. E., et al., 2012, in *Proc. SPIE*. p. 84431A, doi:10.1117/12.926937
- De Marco B., Ponti G., Cappi M., Dadina M., Uttley P., Cackett E. M., Fabian A. C., Miniutti G., 2013, *MNRAS*, 431, 2441
- Fabian A. C., et al., 2009, *Nature*, 459, 540
- Florian M. K., Li N., Gladders M. D., 2016, *ApJ*, 832, 168
- Gallimore J. F., et al., 2016, *ApJ*, 829, L7
- Gandhi P., Hönig S. F., Kishimoto M., 2015, *ApJ*, 812, 113
- García-Burillo S., et al., 2016, *ApJ*, 823, L12
- Ghisellini G., Haardt F., Matt G., 1994, *MNRAS*, 267, 743
- Guainazzi M., Matt G., Perola G. C., 2005, *A&A*, 444, 119
- Haardt F., Maraschi L., 1991, *ApJ*, 380, L51
- Hasinger G., et al., 2001, *A&A*, 365, L45
- Imanishi M., Nakanishi K., Izumi T., 2016, *ApJ*, 822, L10
- Iwasawa K., et al., 1996, *MNRAS*, 282, 1038
- Jansen F., et al., 2001, *A&A*, 365, L1
- Jiang P., Wang J. X., Wang T. G., 2006, *ApJ*, 644, 725

- Just D. W., Brandt W. N., Shemmer O., Steffen A. T., Schneider D. P., Chartas G., Garmire G. P., 2007, *ApJ*, 665, 1004
- Kelly B. C., 2007, *ApJ*, 665, 1489
- King A., Lasota J.-P., 2016, *MNRAS*, 458, L10
- Koss M., et al., 2018, *VizieR Online Data Catalog*,
- Krolik J. H., Madau P., Zycki P. T., 1994, *ApJ*, 420, L57
- Lamer G., McHardy I. M., Uttley P., Jahoda K., 2003, *MNRAS*, 338, 323
- Lanzuisi G., et al., 2014, *ApJ*, 781, 105
- Lehmer B. D., et al., 2019, *ApJS*, 243, 3
- Lusso E., et al., 2010, *A&A*, 512, A34
- Madsen K. K., Beardmore A. P., Forster K., Guainazzi M., Marshall H. L., Miller E. D., Page K. L., Stuhlinger M., 2017, *AJ*, 153, 2
- Marinucci A., Risaliti G., Wang J., Nardini E., Elvis M., Fabbiano G., Bianchi S., Matt G., 2012, *MNRAS*, 423, L6
- Marinucci A., Bianchi S., Fabbiano G., Matt G., Risaliti G., Nardini E., Wang J., 2017, *MNRAS*, 470, 4039
- Marinucci A., Bianchi S., Braito V., Matt G., Nardini E., Reeves J., 2018, *MNRAS*, 478, 5638
- Mushotzky R. F., Fabian A. C., Iwasawa K., Kunieda H., Matsuoka M., Nandra K., Tanaka Y., 1995, *MNRAS*, 272, L9
- Nandra K., 2006, *MNRAS*, 368, L62
- Nayakshin S., Kallman T. R., 2001, *ApJ*, 546, 406
- Nayakshin S., Kazanas D., 2002, *ApJ*, 567, 85
- Nenkova M., Sirocky M. M., Nikutta R., Ivezić Ž., Elitzur M., 2008, *ApJ*, 685, 160

Oh K., et al., 2018, *ApJS*, 235, 4

Paolillo M., Schreier E. J., Giacconi R., Koekemoer A. M., Grogin N. A., 2004, *ApJ*, 611, 93

Papadakis I. E., Chatzopoulos E., Athanasiadis D., Markowitz A., Georgantopoulos I., 2008, *A&A*, 487, 475

Ponti G., et al., 2013, *A&A*, 549, A72

Ricci C., Ueda Y., Koss M. J., Trakhtenbrot B., Bauer F. E., Gandhi P., 2015, *ApJ*, 815, L13

Ross R. R., Fabian A. C., Young A. J., 1999, *MNRAS*, 306, 461

Sánchez P., et al., 2017, *ApJ*, 849, 110

Shakura N. I., Sunyaev R. A., 1973, *A&A*, 500, 33

Shu X. W., Yaqoob T., Wang J. X., 2011, *ApJ*, 738, 147

Steffen A. T., Strateva I., Brandt W. N., Alexander D. M., Koekemoer A. M., Lehmer B. D., Schneider D. P., Vignali C., 2006, *AJ*, 131, 2826

Tanaka Y., Inoue H., Holt S. S., 1994, *PASJ*, 46, L37

Tanaka Y., et al., 1995, *Nature*, 375, 659

Tombesi F., de Marco B., Iwasawa K., Cappi M., Dadina M., Ponti G., Miniutti G., Palumbo G. G. C., 2007, *A&A*, 467, 1057

Vasudevan R. V., Fabian A. C., 2007, *MNRAS*, 381, 1235

Vaughan S., Edelson R., 2001, *ApJ*, 548, 694

Walton D. J., et al., 2013, *ApJ*, 779, 148

Wang J., Fabbiano G., Elvis M., Risaliti G., Mundell C. G., Karovska M., Zezas A., 2011, *ApJ*, 736, 62

Wang J., et al., 2014, *ApJ*, 781, 55

Weisskopf M. C., Tananbaum H. D., Van Speybroeck L. P., O'Dell S. L., 2000, Chandra X-ray Observatory (CXO): overview. pp 2–16, doi:10.1117/12.391545

Winter L. M., Mushotzky R. F., Reynolds C. S., Tueller J., 2009, ApJ, 690, 1322

Yaqoob T., Edelson R., Weaver K. A., Warwick R. S., Mushotzky R. F., Serlemitsos P. J., Holt S. S., 1995, ApJ, 453, L81

Yaqoob T., Serlemitsos P. J., Turner T. J., George I. M., Nandra K., 1996, ApJ, 470, L27

Zhang Z., Gilfanov M., Bogdán Á., 2012, A&A, 546, A36

Zoghbi A., Miller J. M., Cackett E., 2019, ApJ, 884, 26

Appendix A

Light curves

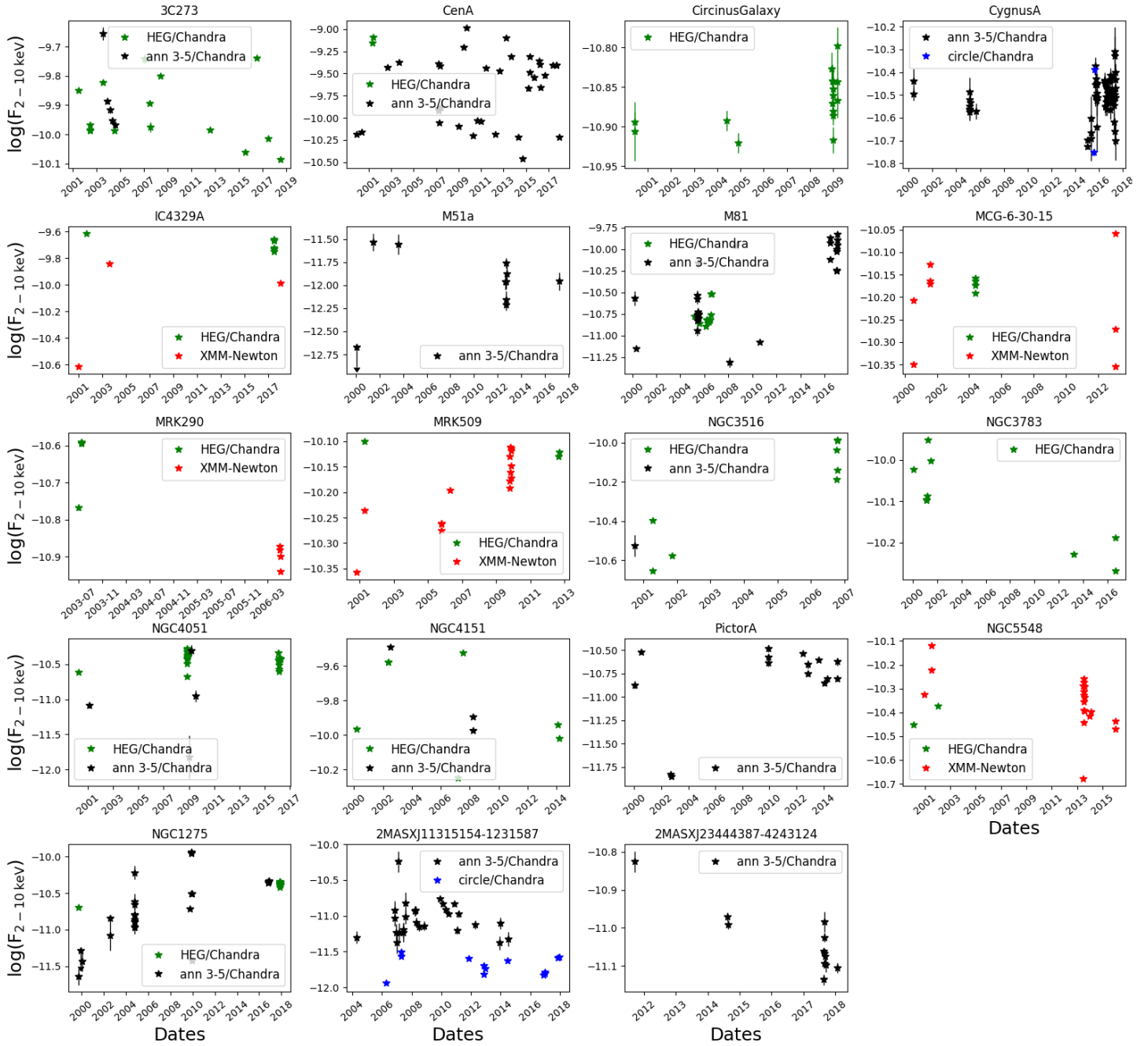


Figure A.1: Light curves for the 2–10 keV continuum flux ($F_{2-10 \text{ keV}}$) for the sources with well-constrained $F_{6.4 \text{ keV}}-F_{2-10 \text{ keV}}$ slopes. In the subplots, the green stars are the *Chandra* HEG spectra, the black stars are the *Chandra* ACIS 3''–5'' annular spectra, the blue stars are the 1.5'' circular ACIS spectra and the red stars are the *XMM-Newton* spectra. The unities of the flux are $\text{erg cm}^{-2} \text{s}^{-1}$

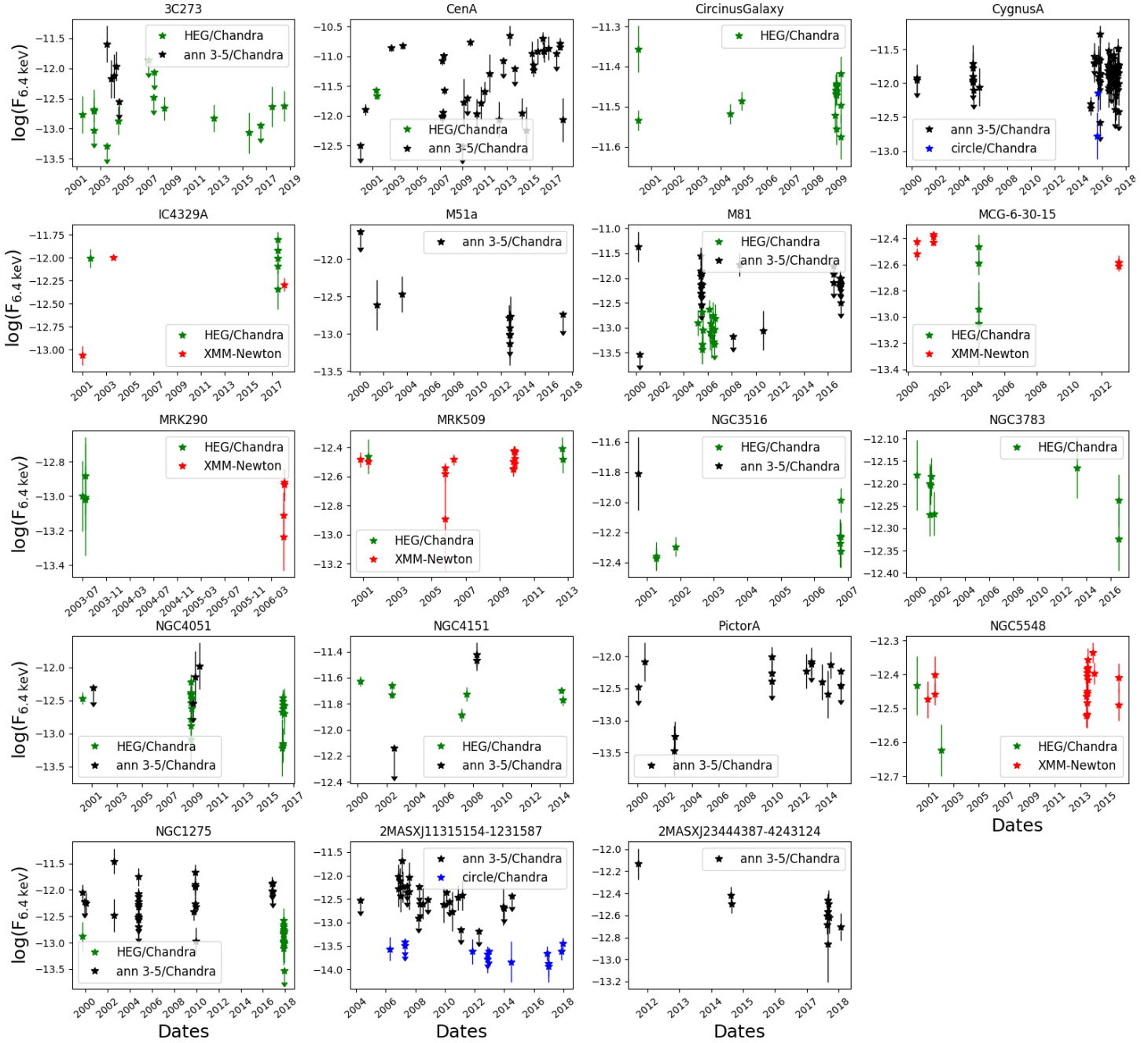


Figure A.2: Light curves for the Fe $K\alpha$ line flux ($F_{2-10\text{ keV}}$) for the sources with well-constrained $F_{6.4\text{ keV}}-F_{2-10\text{ keV}}$. In the subplots, the green stars are the *Chandra* HEG spectra, the black stars are the *Chandra* ACIS 3''–5'' annular spectra, the blue stars are the 1.5'' circular ACIS spectra and the red stars are the *XMM-Newton* spectra. The unities of the flux are $\text{erg cm}^{-2} \text{s}^{-1}$

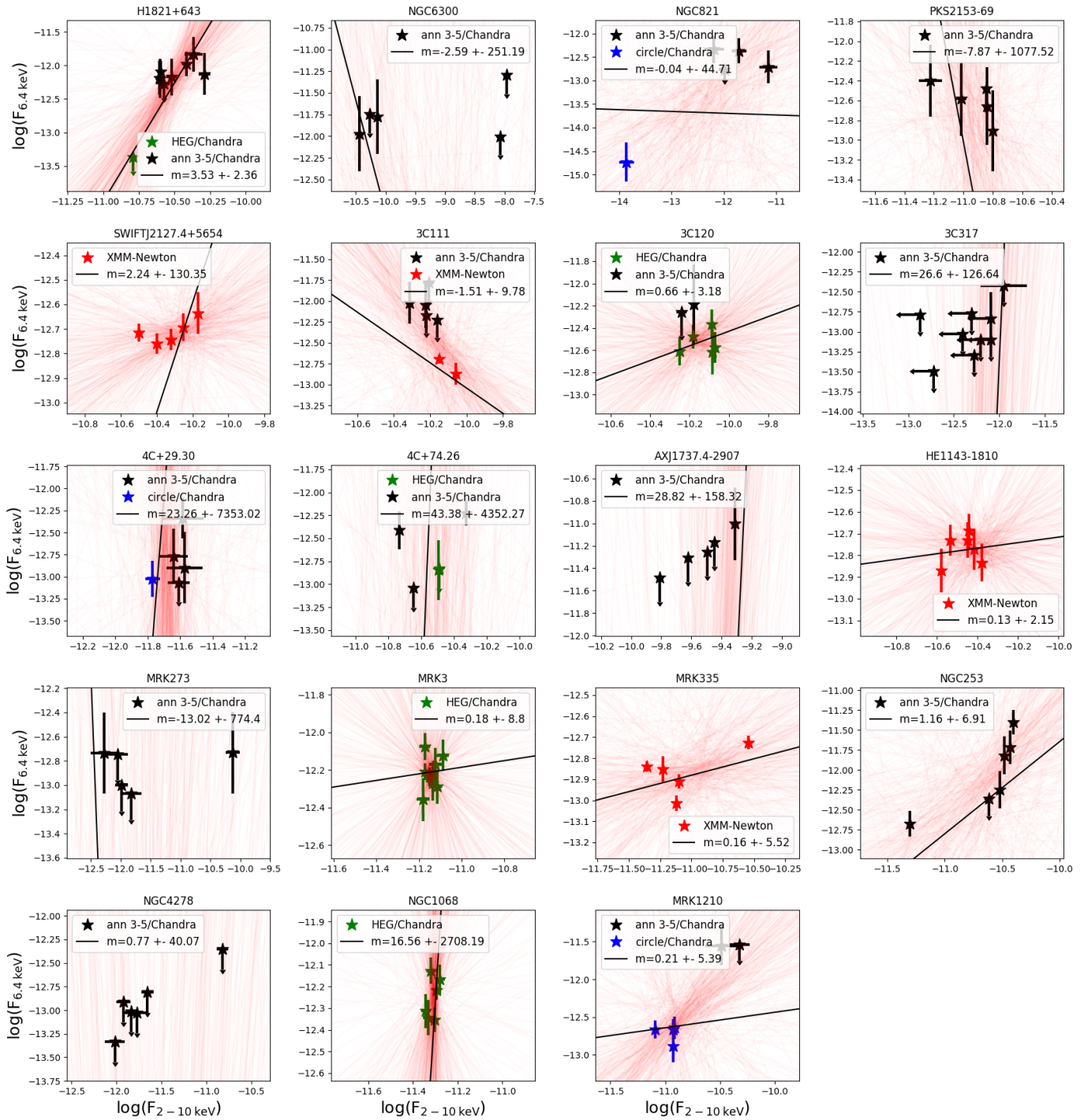


Figure A.3: Same as Figure 3.1 but for the sources with unconstrained $F_{6.4 \text{ keV}}-F_{2-10 \text{ keV}}$ slopes. The value of the slope (m) is in the legend of each source

Appendix B

Radial profiles

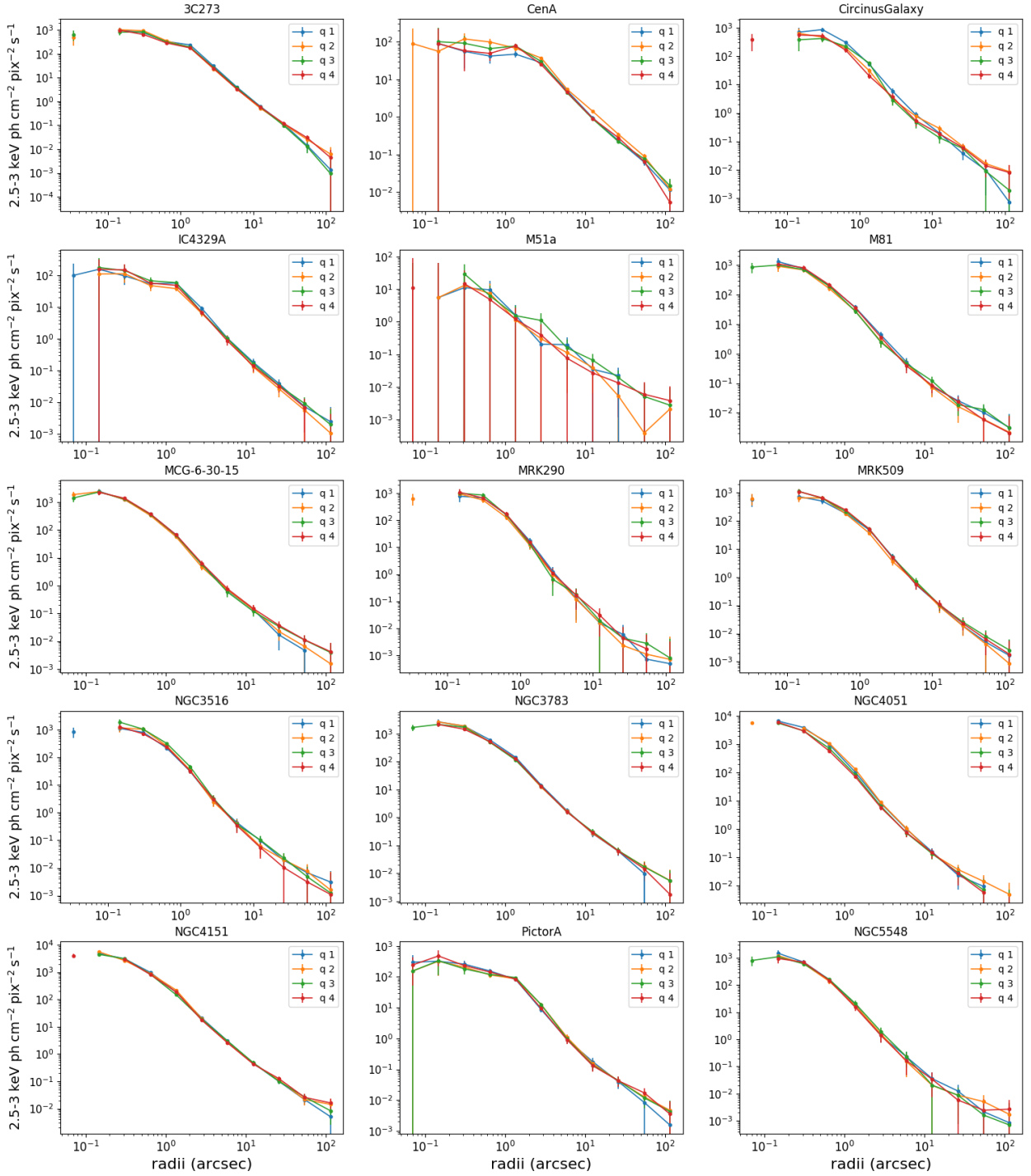


Figure B.1: Radial profiles for each quadrant of the images of all the sources with well-constrained $F_{6.4\text{ keV}} - F_{2-10\text{ keV}}$ slopes (except the ones with difficult contamination subtraction). The profiles are for the flux in the 2.5–3 keV range. q1, q2, q3 and q4 are equivalent to quadrant I, quadrant II, quadrant III and quadrant IV. The errors plotted are 3-sigma confidence.

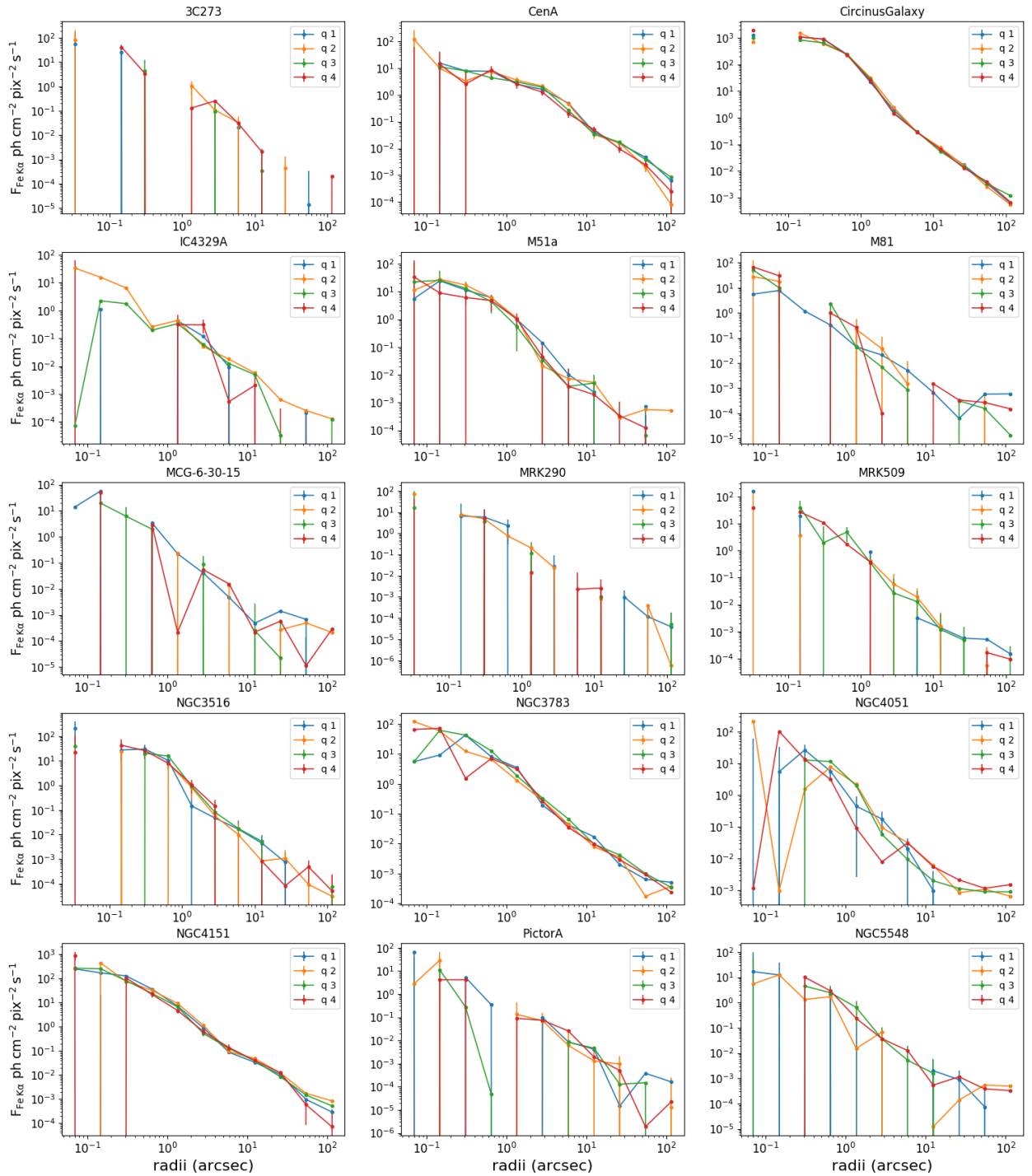


Figure B.2: Same as Figure B.1, but for the Fe $K\alpha$ line photons

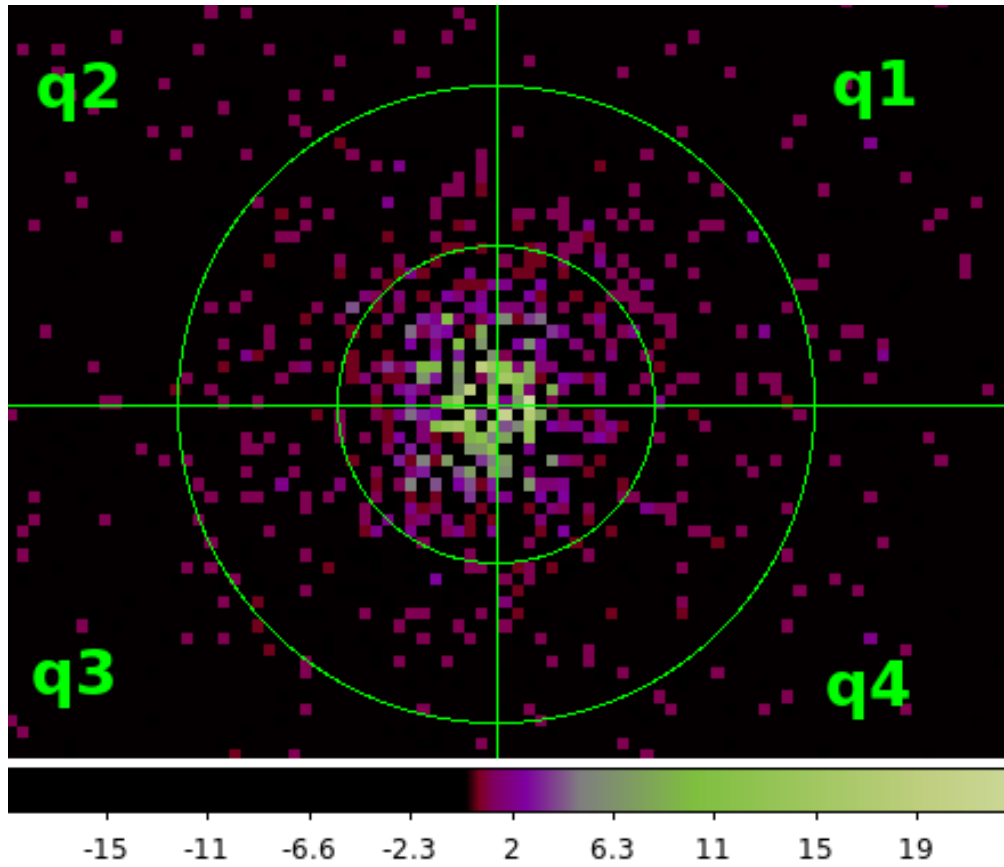


Figure B.3: Image for the Fe K α line photon of NGC 4051. The quadrants are pointed in the image. The circles mark radii of 2'' and 4''.

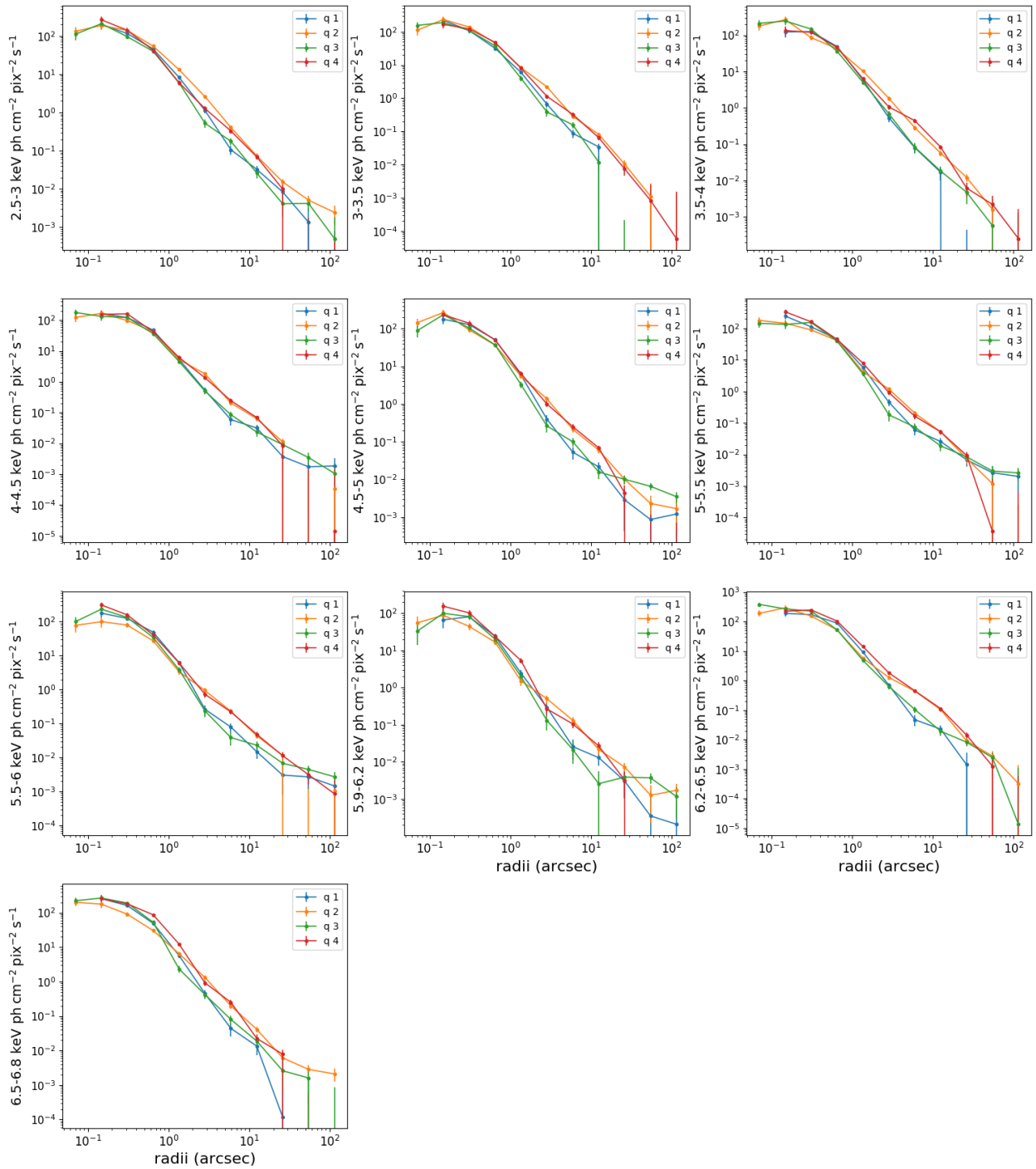


Figure B.4: Radial profiles for each quadrant of the images of NGC 1068, for different energy ranges, going from 2.5–3 keV to 6.5–6.8 keV